

# THE IMPACT OF FEEDBACK-DRIVEN OUTFLOWS ON BAR FORMATION

MARTIN D. WEINBERG

Astronomy Department, University of Massachusetts, Amherst, MA 01003

Version June 13, 2025

## ABSTRACT

We investigate the coupling between the temporal variation from central mass outflows and the bar instability. We show that gravitational fluctuations from AGN-driven mass outflows affect the radial motion of disk orbits. The resulting incoherence in orbital phase leads to the disruption of the bar-forming dynamics. Bar formation is suppressed in galaxies with repeated outflow events separated by  $10 < \tau < 200$  Myr with wind mass  $\sim 15\%$  of the disk within  $\sim 0.5$  scale lengths or  $1.4\%$  of the total disk mass. The work done by central AGN feedback is capable of reducing the amplitude or, with enough amplitude, destroying an existing bar. Conversely, SF feedback that is distributed across the disk has insufficient spatial and temporal coherence to suppress bar formation.

To model the dynamics of the coupling and interpret the results of the full N-body simulations, we introduce a generalization of the Hamiltonian mean-field (HMF) model, drawing inspiration from the Lynden-Bell (1979) mechanism for bar growth. Our non-linear *BarHMF* model is designed to reproduce linear perturbation theory in the low-amplitude limit. Without feedback, this model exhibits exponential growth whose rate depends on disk mass and reproduces the expected saturation of bar growth observed in N-body simulations. We describe several promising applications of the BarHMF model beyond this study.

*Subject headings:* galaxies: evolution – galaxies: halos – galaxies: kinematics and dynamics – galaxies: structure.

## 1. INTRODUCTION

### 1.1. Background

Bar are a ubiquitous feature of disk galaxies: at least 50% of all disk galaxies in the local universe are barred (e.g. Aguerri *et al.* 2009). Bars were among the first instabilities to be found and studied in N-body simulations (Hohl 1971; Ostriker and Peebles 1973). They are predicted to be important drivers of secular evolution (Lynden-Bell and Kalnajs 1972; Tremaine and Weinberg 1984) and barred galaxies may *require* secular evolution to create their present-day morphology (Athanasoula 2003). In this way, their coupling to the baryonic, and the dark-matter components of a galaxy through cosmic time make their dynamical details an important diagnostic of galaxy formation and evolution. A significant fraction of the stellar disk takes part in the bar instability, making bars morphologically distinct and straightforwardly observed in the near-infrared. Indeed, recent analyses of JWST NIRC*am* images suggest that some bar systems may have been active for many gigayears (Guo *et al.* 2023). An understanding of the formation time and duty cycle of bar-driven evolution requires a thorough understanding of the dynamical mechanisms that affect bar evolution.

Both by technical necessity and experimental design, most theoretical and numerical studies of barred galaxy dynamics begin with quiescent equilibria chosen to be unstable to bar formation. Some of the dynamical principles governing bar formation and subsequent secular evolution are well-understood after decades of study (see

Binney and Tremaine 2008). While our dynamical insight follows from such carefully controlled dynamical experiments (e.g. Petersen *et al.* 2019, 2021), we are well-aware that galaxies continue to accrete and lose mass through cosmic time, but we have not given this time dependence detailed attention dynamically. In particular, a wide variety of time-dependent feedback processes are necessary to produce the galaxies in cosmological simulations (e.g. Ceverino and Klypin 2009; Kormendy and Ho 2013). For example, the work done on the gravitational potential by this feedback has a natural time scale and amplitude. The time scale is approximately 10–200 Myr based on theory and estimated from observations (Heckman *et al.* 1990; Hopkins and Hernquist 2010). The amount of mass lost from the disk, and hence work done on the disk gravitational potential is much harder to estimate. Star formation efficiencies in a star forming event are estimated to be  $\mathcal{O}(0.1)$  and estimates of mass outflow rates from AGN feedback range from 1 to 5 times the star formation rate (Combes *et al.* 2013; Combes 2017).

The bar instability itself results from the precession of apocenter positions of nearby orbits toward its self-induced quadrupole distortion. If a non-trivial fraction of the remaining gas is heated or launched into halo during an AGN outburst or strong star-formation event, the work done on the gravitational potential changes the orbital actions of stars in the disk. These event time scales are similar to the characteristic orbital times in the disk. Thus, the resulting mass-outflow-driven fluctuations can affect the orbital coherence required for bar formation. We expect this coupling to be particularly important dur-

ing at redshifts of  $z = 2\text{--}3$  often called *cosmic noon*. During this rapid baryonic accretion phase, galaxies formed about half of their current stellar mass (Madau and Dickinson 2014), gas advection will be strong efficiently feeding central super-massive black holes (SMBHs), and the effect of feedback will be maximal and most likely significant source of gravitational fluctuations. While widely explored in suites of galaxy-formation simulations, the details of multi-scale physical processes are not well determined. An overall, general description of the coupling between the feedback fluctuations and the bar instability mechanism and estimating the importance of feedback to bar formation is the main goal of this paper.

### 1.2. Feedback processes

There are two main feedback mechanisms in cosmological simulations that have regulatory affect on the baryonic history: active galactic nuclei (AGN) and star formation (SF). Presumably, both play a role in the self regulation necessary to achieve the observed characteristics of present day galaxies. Both AGN winds and the interaction of supernova feedback with their surrounding gas through the injection of energy and momentum can lead to a feedback loop regulating ongoing evolution and outflow. An effective feedback loop requires removing a large fraction of the disk’s cold gas by winds, heating and fountains. A variety of sub-resolution prescriptions have been employed to achieve this. Regardless of the details of the microphysics, these outflow events are episodic, not continuous. Because these events tend to be centrally dominated with a cadence of  $10 < \tau < 200$  Myr, outflow events will provide gravitational fluctuations on dynamical timescales to the axisymmetric field of the disk. Similar to the regulation by feedback, the mass in the outflow need not escape from the galaxy to have affect on bar dynamics since most of the gravitational work occurs over the first kiloparsec.

Feedback processes and galactic winds specifically have been well-reviewed over many years (e.g. Veilleux *et al.* 2005; King and Pounds 2015; Zhang 2018). The importance of the physical details in modeling SF regulation is also well appreciated. For example, Governato *et al.* (2007) remarked that subgrid star formation feedback tended to make the disk more stable against bar formation by reducing the mass of the disk. Since then, simulations with higher resolution and sophisticated subgrid prescriptions have demonstrated large variance and intricate coupling between outflow, re-accretion of gas, and subsequent star formation with bar formation, even in the same simulation suite Zana *et al.* (e.g. 2019).

### 1.3. Coupling to disk bars and caveats

The goal of this paper is a characterization of the coupling between feedback-induced fluctuations in the gravitational field and the galactic dynamics of bar formation. The proposed model is very simple and crude by today’s standards for *subgrid* physics in cosmological simulations. It is a simple Markov jump process for central feedback-driven outflow. This models feedback as a sudden loss of mass at Poisson-process intervals with an exponential replenishment time. Thus, the disk mass remains constant on average without explicitly following the mass settling or reaccretion itself.

We then investigate the fluctuation amplitude and time scales parametrized by this simple model that are required to disrupt bar formation. We choose an exponential disk and live dark-matter halo with masses typical of typical of a Milky-Way-like galaxy at *cosmic noon* for our simulations.

The background model adopted for this study is not intended to be realistic in the cosmological structure formation sense; neither our disk or halo accretes new material in time. For this reason, we focus on evolution times  $< 4$  Gyr. Similarly, our simulations do not include satellite and sub-structure interactions. We emphasize that our feedback process is no more than a *fitting formula*; it does not consider the physical mass-loss time scale or the impact of the feedback on the structure or populations in the disk. Rather, this suite is intended explore the dynamics of the coupling mechanism and to address two particular questions: (1) What is the stochastic frequency required to disrupt bar formation? (2) What is the amplitude of the work done required to disrupt bar formation? While inspired by feedback, the proposed dynamical mechanism is generic and intended to provide a framework for interpreting more realistic simulations. The mechanism proposed here has thematic overlap with the suggestion by Ogiya and Mori (2014) that resonant coupling between a feedback-excited density wave can promote the cusp-core transition. The main dynamical difference is we couple the gravitational field fluctuation from a stochastic outflow directly to the dynamics of bar orbits.

Our *primary* galaxy model forms a bar in the absence of potential fluctuations with a disk mass of approximately  $M_{disk} = 5 \times 10^9 M_{\odot}$  with  $M_{halo} = 10^{12} M_{\odot}$ . The system is not strongly bar unstable owing to its relatively low, *sub-maximal* disk mass. We intentionally choose a bulge-free model with a rising rotation curve inside of 6 kpc to promote bar formation within a few gigayears. Both growth rates and subsequent pattern speed changes will be model dependent. We show that bar formation is suppressed for strong central outflows with characteristic periods in the range  $10 < \tau < 200$  Myr. Sufficient *blow out* amplitude is approximately 15% of the baryonic mass inside of 0.5 disk scale lengths. Our super-bubble model (Kipper *et al.* 2025) *does not* suppress bar formation for parameters typical of starburst rates. This suggests that large-scale central outflows are necessary for the dynamical model to be effective.

### 1.4. A theoretical bar model

To provide dynamical insight for the feedback coupling to bar dynamics, we present a new hybrid perturbation-theory-based simulation. Specifically, we adopt the tools of Hamiltonian perturbation theory to isolate the single degree of freedom that causes the outer apsides of disk orbits to collect along a diameter. This is the bar-formation mechanism described in Lynden-Bell (1979). This isolation is derived by performing a change of angular coordinates where one of the angles describes the motion with respect to the inner-Lindblad resonance. Near resonance, the angular speed of this angle is much slower than the rapid variation of the star about its orbit radially. This allows us to average of the radial motion and reduce the dimensionality of the equations of motion. Appendix B develops this idea into a particle simulation

method. Although based on linear perturbation theory, the coupling is nonlinear and related to the Hamiltonian Mean Field model (e.g. Chavanis *et al.* 2005). This allows investigation of both the linear and nonlinear phases of bar growth. We use this model in Section 3.4.4 to verify the dynamical interaction between feedback and bar formation.

### 1.5. Plan

The plan for this paper is as follows. Section 2 describes our galaxy mass profiles (Sec. 2.1), summarizes our N-body simulations of the disk and halo (Sec. 2.2), defines the parametrization of the feedback mechanisms for both central AGN-type and spatially distributed SF-type outflows (Sec. 2.4), and describes the new hybrid perturbation-theory based simulation (Sec. 2.5). The results are described in Section 3, beginning with a demonstration of the main result in Section 3.3 followed description of the primary model without feedback in Section 3.2. Sections 3.4.1 and 3.4.2 describe the amplitudes and frequencies of the feedback process necessary to suppress the bar instability. Section 3.4.4 presents a dynamical mechanism for the noise coupling in the reduced model and compares it to the results from the full N-body simulations. We conclude with a summary and discussion in Section 4.

## 2. METHODS

### 2.1. Galaxy model

We use *virial* units for length and mass,  $R_{vir}$  and  $M_{vir}$  respectively, with gravitational constant  $G = 1$  for all simulations described here and refer to those as *system units*. We present our results scaled to the Milky Way throughout to give physical context. We adopt  $R_{vir} = 300$  kpc and  $M_{vir} = 1.4 \times 10^{12} M_{\odot}$  and use gigayears (Gyr) for time units. The system time units are  $T_{vir} \equiv (R_{vir}^3/GM_{vir})^{1/2} \approx 2$  Gyr; or 1 Gyr is approximately 0.5 system time units.

#### 2.1.1. Dark-matter halo

For our primary model, we adopt a modified NFW (Navarro *et al.* 1997) dark matter halo with concentration  $c$ , whose density is given by

$$\rho_{\text{halo}}(r) \propto (r + r_c)^{-1} (r + r_s)^{-2} \quad (1)$$

where  $r_s \equiv R_{vir}/c$  is the scale radius, and  $r_c \ll r_s$  is a radius that sets the size of the core. In this paper, the core radius is numerical convenience only and set to a value smaller than any astronomically relevant scale, typically several parsecs. We adopt  $c = 15$  for our dark matter halo which provides an acceptable representation of the rotation curve when scaled to the Milky Way. This is slightly more concentrated than the mean from Diemer and Kravtsov (2015) but within the variance measured from simulations.

In practice, we choose a more general profile family that includes the NFW model to explore the dynamical effect of changing the background profile from shallow to steep and enforce a finite total mass. Specifically, we modify a two-power halo model with an error function

truncation of the following form:

$$\rho_{\alpha\beta}(r) = \frac{\rho_0 r_s^{\alpha+\beta}}{(r + r_c)^{\alpha}(r + r_s)^{\beta}} \left\{ \frac{1 + \text{erf}[(r_t - r)/r_w]}{2} \right\}. \quad (2)$$

where  $\rho_0$  is a normalization set by the chosen mass. This is equivalent to equation (1) for  $\alpha = 1$  and  $\beta = 2$ , and  $r_t = \infty$ . The outer truncation radius  $r_t$  and truncation width  $r_w$  are chosen to be 300 kpc and 60 kpc, respectively. For our primary model, we set  $\alpha = 1$ ,  $\beta = 2$ ,  $r_c = 4.5$  pc. We explore the effect of different  $\alpha$  in Appendix B.4.

While one may debate the merits of a purely collisionless dark matter particle, axion dark matter, ‘fuzzy’ dark matter (Hu *et al.* 2000; Hui *et al.* 2017), or other descriptions of dark matter, the necessity of exploring the interaction between baryonic and unseen components via gravity may not be ignored. Dark matter will respond gravitationally to baryonic matter and different dark-matter responses can produce observable signatures. Rigidity in halos has been noted to limit bar growth (Polyachenko *et al.* 2016; Sellwood 2016) as is clear from dynamics of secular evolution (Athanassoula 2003), and so we emphasize that the live halo inclusion is crucial to recover the dynamics of the standard  $\Lambda$ CDM scenario. Specifically, both the fraction of gravitational support from the halo and the resonant coupling will affect bar growth, although we will not explore that sensitivity in this paper. There are many other parameters that may be adjusted in the creation of a halo which we do not explore here: triaxiality and spin are two that are addressed by others (Athanassoula *et al.* 2013; Aumer *et al.* 2016; Collier *et al.* 2018a,b). However, we do not expect either of these to qualitatively change the dynamical features explored in this work.

#### 2.1.2. Disk

The simulations begin with an exponential disk of surface density

$$\Sigma_{\text{disk}}(r) = \frac{M_d}{2\pi a^2} \exp\left(-\frac{r}{a}\right) \quad (3)$$

where  $M_d$  is the disk mass, and  $a \equiv 0.01R_{vir} = 3$  kpc is the disk scale length. We assume that the disk remains thin with no vertical response to further restrict the dynamical degrees of freedom for this simple proof-of-concept investigation. This is often called the *razor-thin* limit. We have repeated a small set of key simulations described in Section 3.1 with a full three-dimensional disk and the results are nearly identical, as expected.

We select the initial positions in the disk via acceptance-rejection algorithm using equation (3). We select the velocities by solving the Jeans equations (Binney and Tremaine 2008) with an axisymmetric velocity ellipsoid in the disk plane ( $\sigma_r \equiv \sigma_{\phi}$ ). We characterize the radial velocity dispersion using the Toomre  $Q$  parameter,

$$\sigma_r^2(r) = \frac{3.36\Sigma(r)Q}{\Omega_r(r)} \quad (4)$$

where  $\Sigma(r)$  is the disk surface density, and the radial frequency,  $\Omega_r$ , is given by

$$\Omega_r^2(r) = r \frac{d\Omega_{\phi}^2}{dr} + 4\Omega_{\phi}^2. \quad (5)$$

where  $\Omega_\phi$  is the azimuthal frequency. See Section 2.3 for additional details. The circular velocity curve for this model is shown in Figure 4. The rise in the inner few kiloparsecs promotes bar growth by design.

### 2.2. *N*-body method

The BFE method for *N*-body simulation uses a basis of *biorthogonal function* pairs constructed from the eigenfunctions of the Laplacian. The pair solves the Poisson equation,  $\nabla^2\Phi_j = 4\pi G\rho_j$ , with the inner product  $(\Phi_j, \rho_k) \propto \delta_{jk}$ . Projecting the density distribution implied by an ensemble of point-positions onto the basis yields the gravitational potential. Forces immediately follow. This method was introduced by (Clutton-Brock 1972), inspired by the mathematical tools used for the joint analytic solution of the collisionless Boltzmann equation and the Poisson equation. (Clutton-Brock 1972, 1973; Hernquist and Ostriker 1992) all derive recursion relations for biorthogonal bases using various transformations and sets of special functions. This method has the practical advantage of automatically filtering variations in the field to the largest spatial scales. We choose a fixed number of basis functions to represent structural features on characteristic scales much larger than the inter-particle spacing such as arms and bars in the disk and dark-matter wakes in the halo. The resulting algorithm has computational complexity  $\mathcal{O}(N)$ ; that is, gravitational field evaluation scales linearly with particle number. The main disadvantage of this approach is that it lacks general flexibility and depends on an expansion center. Nonetheless, it is an excellent choice for studying the evolution of systems to modest perturbations.

Weinberg (1999) proposed a numerical solution of the underlying Sturm-Liouville equation to construct eigenfunctions whose lowest-order basis function pair matches the desired background equilibrium system. This extends the flexibility of the BFE approach by widening the suitable family of equilibrium models to cover cases that did not match the available recursion-relation bases. The full method is described precisely in Petersen *et al.* (2022). This approach along with a suite of analysis tools tailored to BFE simulations is implemented in EXP (Petersen and Weinberg 2025), our publicly available BFE *N*-body and analysis code.<sup>1</sup> We implement bases for a variety of geometries, including spherical, two- and three-dimensional cylindrical, slabs, and rectangular boxes.

For the spherical case, EXP optimally represents the BFE with radial basis functions determined by the target density profile and spherical harmonics. The lowest-order  $l = 0, m = 0$  basis function matches the potential and density of the equilibrium. The overall fields of the halo are described by  $(l_{\text{halo}} + 1)^2 \times n_{\text{halo}}$  terms, where  $l_{\text{halo}}$  is the maximum order of spherical harmonics and  $n_{\text{halo}}$  is the maximum order of radial terms per  $l$  order. For simulations and analyses in this paper, we use a maximum harmonic order  $l_{\text{max}} = 6$  and maximum radial order  $n_{\text{max}} = 20$  using the Sturm-Liouville basis conditioned on each particular input model. While the quality of the expansion is center dependent, the basis can

follow any displacement from the center for sufficiently large particle number and large values of  $l_{\text{max}}$  and  $n_{\text{max}}$ . The choices of  $l_{\text{max}} = 6$  and  $n_{\text{max}} = 20$  allow us follow the small center displacements seen in our simulations. A discussion of convergence for the NFW halo used here is found in Petersen *et al.* (2022, Section 3). The resulting series of coefficients fully describe time dependence of the gravitational field produced by the *N*-body evolution<sup>2</sup>.

Appropriate basis functions for a three-dimensional cylindrical disk are described in Petersen *et al.* (2022, Section 3) along with a study of convergence properties. Here, we use a recently-implemented special-purpose two-dimensional cylindrical disk basis that is described in Appendix A. The method and performance well described by the Petersen *et al.* (2022) study restricted to  $z = 0$ . This focuses our dynamical attention on the two degrees of freedom essential to create a bar: the radial and azimuthal motion. We have demonstrated that same results are obtained for the full three-dimensional simulations in selected cases. Future work will include coupling to the vertical motion from possibly asymmetric outflows.

In summary, EXP allows for a straightforward calculation of the gravitational potential from the mass distribution through time. The key limitation of the BFE method lies in the loss of flexibility owing to the truncation of the expansion series: large deviations from the equilibrium disk or halo will not be well represented. Although the basis is formally complete, our truncated version limits the variations that can be accurately reconstructed. Despite this, basis functions can be a powerful tool to gain physical insight; analogous to traditional Fourier analysis, a BFE identifies spatial scales and locations responsible for the model evolution. In particular, this paper investigates relatively low-amplitude, large-scale distortions which are well represented by the expansion.

### 2.3. *Initial conditions*

We generate realizations with  $10^6$  disk particles and  $10^7$  halo particles from the models in Sections 2.1.1 and 2.1.2 using the following algorithm:

1. The halo gravitational potential is modified to contain the monopole component of the exponential disk. The halo phase space distribution is then realized using Eddington inversion (e.g. Binney and Tremaine 2008). This helps improve the initial equilibrium.
2. The disk phase space is generated using Jeans' equations as described in Section 2.1.2. Gaussian velocity selection rather than velocity selection from the exact phase-space distribution function will introduce disequilibrium to start. This is mitigated by the relaxation in Step 5 described below.
3. The halo phase-space distribution is *relaxed* in the presence of the potential generated by the disk particle distribution using the EXP potential solver for

<sup>1</sup> The EXP code suite is publicly available on GitHub (see <https://github.com/EXP-code/EXP.git>) and full documentation is available from ReadTheDocs (see <https://expdocs.readthedocs.io>).

<sup>2</sup> This method will work for triaxial halos as well. For triaxial halos, the target density can be chosen to be a close fitting spherical approximation of the triaxial model. The equilibrium will require non-axisymmetric terms but the series will converge quickly.

- 4 Gyr ( $2T_{vir}$ ). The force felt by the halo from the halo's own self gravity is restricted to  $m = 0$  terms during this relaxation phase. The force felt by the halo from the disk is the disk's gravity at  $T = 0$  for the axisymmetric component  $m = 0$  only.
4. The disk phase space is regenerated using Jeans' equations as described in Section 2.1.2 using the gravitational potential of the halo distribution at the end of the relaxation step.
  5. The disk phase-space distribution is then relaxed in the presence of the potential generated by the halo particle distribution using the EXP potential solver for 4 Gyr. The force felt by the disk from the disk's own self gravity is restricted to the  $m = 0$  term. The force felt by the disk from the halo is the halo's gravity for the  $m = 0$  axisymmetric component only frozen at the beginning of this simulation.
  6. The phase space distributions for the halo at the end of Step 3 and the disk at the end of Step 5 are the phase-space initial conditions for the simulations reported here.

This algorithm is enabled by the basis-function approach that underlies EXP. In particular, the BFE approach used in EXP provides a separate basis for each component (disk and halo, here) and each the expansion terms for basis may be applied selectively or frozen in time. For example, in Step 3 we allow only the axisymmetric force of the halo to obtain the new *spheroidal* equilibrium in the presence of the disk while preventing the natural halo modes from influencing the initial conditions. The resulting initial conditions are very close to feature-free to start. The initial condition realization described here has also been discussed in Petersen *et al.* (2022).

#### 2.4. Perturbation scheme

We describe each of our two stochastic outflow models below. In Section 2.4.1, we simulate a central outflow, applicable to both an AGN or nuclear superwind (Romero *et al.* 2018), by modulating the mass of the stars according to a specific schedule that is tracked by the particles themselves. This could equally well have been implemented with negative mass disk-shaped particles that projected on the expansion coefficients directly. We implemented this coefficient projection scheme as a check on particle-mass adjustment algorithm and obtained similar results. To simulate the typical SF outflow process in a more realistic way, we implement diffuse gas bubbles with the spatial distribution of a snowplow-phase mass shell (Section 2.4.2). A suite of simulations suggests that these super bubbles have very little effect on bar formation for astronomically-relevant parameters, suggesting that the central fluctuation of the global gravitational potential is a necessary for effective coupling to the bar instability.

##### 2.4.1. The central outflow model (AGN)

We assume that an AGN or nuclear starburst can be modeled as a stochastic process in the inner galaxy disk that causes a sudden loss of fraction  $\epsilon$  of the enclosed mass within radius  $R_{burst} \equiv \lambda a$  where  $a$  is the disk scale

length. In other words, mass from the outflow is lost from an inner disk with radius  $\lambda a$ . Experiments performed as part of Section 3 show that the dynamical effect of the mass loss is only weakly dependent on  $\lambda$  for  $\lambda \lesssim 0.5$ . The lost mass is assumed to be fall back onto the disk over some characteristic period  $P_{acc}$ . This emulates a radiatively driven outflow and the subsequent resettling of cooling gas. The perturbation is modeled mathematically as a Markov jump process with two characteristic frequencies: one that describes the outburst frequency,  $1/\tau_1$ , and one that describes the settling time,  $\tau_2 = P_{acc}$ . Let  $\tau_{dyn}$  be the dynamic time scale. Physical consistency implies that  $\tau_{dyn} \lesssim \tau_2$ .

The algorithm is implemented in EXP as follows:

1. Let  $t$  be the current simulation time and let  $t_*$  be the time at the last outflow event. At every time step, an outflow event occurs with exponential probability (Poisson)

$$P(t) = e^{-(t-t_*)/\tau_1}. \quad (6)$$

This implies that the likelihood of a new event at the current time  $t$  is  $P(t > t_*) = 1 - e^{-(t-t_*)/\tau_1}$ . Therefore, we may randomly generate the time for the next event as  $t_+ = t_* - \tau_1 \log(\mathcal{R})$  where  $\mathcal{R}$  is a random variate in  $(0, 1]$ .

2. An event occurs when  $t \geq t_+$ . At that time, all star particles within radius  $\lambda a$  lose a fraction of their mass,  $\epsilon$ . We set the particle event time  $t_+ \rightarrow t_*$ . Each star particle carries the time of its last event.
3. Each star gains back mass according to:

$$m = m_o \left[ 1 - \epsilon e^{-(t-t_*)/\tau_2} \right], \quad (7)$$

where  $m_o$  is the mass of the star at  $t = 0$ .

4. At the start, we choose  $t_+ = -\tau_1 \log(\mathcal{R})$  and  $t_* = -\infty$  for all particles. This implies that the mass per star particle ranges between  $(1-\epsilon)m_o$  and  $m_o$  and is  $m_o$  to start. We emphasize that changing the mass per particle is a device to adjust the gravitational profile of the inner galaxy. The individual trajectories only change through this mass adjustment to the mean gravitational field.
5. The AGN or central event frequency,  $1/\tau_1$  and the mass replenishment time,  $\tau_2$ , may be different. For results reported here, we assume that  $\tau_2 = \tau_1/2$  so that the disk recovers most of its mass on average before the next AGN event<sup>3</sup>. Tests show that the end results are very weakly dependent on the precise value of  $\tau_2$  for  $\tau_2 = \mathcal{O}(\tau_1)$ .

To reiterate, this algorithm conserves mass over long time intervals; we assume that some process exists to return

<sup>3</sup> Our model demands  $\tau_2 < \tau_1$  to represent a fluctuating quantity; for  $\tau_2 \gg \tau_1$ ,  $m \rightarrow m_o(1-\epsilon)$  and remains nearly constant. However, if  $\tau_2$  is much smaller than a orbital time, the mass resettles before stellar trajectories can be affected by the change in gravity. This time scale is limited from below by the outflow wind speed, which is typically no more than five times the typical circular velocity. Similarly,  $\tau_1$  is typically less than an orbital time. This implies that  $\tau_{dyn} \lesssim \tau_2 \lesssim \tau_1$ .

the *lost mass* to disk for  $\tau \gg \tau_2$ . This may through accretion of hot halo gas or the settling of a galactic fountain gas. In any case, the mass loss rate

$$\dot{M}_{loss} = M_d(\lambda a)\epsilon/\tau_1,$$

where

$$M_d(R) = M_d \left[ 1 - (1 + R/a)e^{-R/a} \right],$$

may be larger than the typical mass-loss rate measured in galaxy winds. The gravitational fluctuation resulting from this mass loss scales as  $GM_d\epsilon/a$ . Any variation in  $\lambda$  is equivalent to a fixed value of  $\lambda$  and a commensurate variation in  $\epsilon$ . Therefore, we assume a fiducial value,  $\lambda = 2/3$ , for many of the runs considered here with  $M_d = 5 \times 10^9 M_\odot$ . This implies that the mass affected by feedback is

$$M_d(2a/3) = 0.144M_d\epsilon \quad (8)$$

and the mass loss occurs in the inner 2 kpc of the galaxy. As an astronomical parameter, this radius is unrealistically large for an actual AGN-driven outflow. However, the axisymmetric ( $m = 0$ ) component of force felt by the trajectories that comprise the bar are dominated by the lowest order terms in the  $m = 0$  expansion. Decreasing  $\lambda$  tends to increase the change in the higher order terms and but not affect the change from mass loss in the lower-order terms. This explains the measured insensitivity to smaller values of  $\lambda$ . A larger value of  $\lambda$  allows the change in the gravitational field to be well-resolved by the basis function expansion.

As an internal check, we also include the work done by an outflow wind by replacing Steps (2)-(4) in the algorithm by a direct modification of the gravitational field expansion coefficients as follows. When an event occurs at time  $t_j$ , we create a negative mass disk with radius  $\lambda a$  and surface density

$$\Sigma_\epsilon(t) = -\epsilon \frac{M_d(\lambda a)}{\pi(\lambda a)^2} e^{-(t-t_*)/\tau_2}. \quad (9)$$

The BFE coefficients describing this mass outflow are

$$\delta a_k^\epsilon(t) = 2\pi\Sigma_\epsilon(t) \int_0^{\lambda a} dr r \Phi_{0k}^*(r) \quad (10)$$

following the development in Appendix A. These  $\delta \mathbf{a}^\epsilon(t)$  values are added to the field expansion coefficients from the particles in the simulation. The value of  $t_*$  is updated whenever an event occurs. We repeated the simulations for a number of cases described in Section 3.1 with no significant changes to the bar formation trends.

#### 2.4.2. The super-bubble model (SF)

The mechanism from Section 2.4.1 describes a stochastic loss of mass that does work on the center of a disk galaxy. We consider an alternative model inspired by the SF process specifically: super-bubble creation by strong SF events scattered throughout the galaxy disk. We model super-bubbles as spherical shells of gas describing the late-time snowplow phase of a supernova cluster. Kipper *et al.* (2025) describes and models the density profile and time dependence of super bubbles based on Yadav *et al.* (2017) and MHD simulations from Kim and Ostriker (2017). Their model includes the evolution of

the bubble in both space and time. For easy of implementation, we implement a simplified version of their super-bubble model as a time-static profile with a temporally evolving amplitude.

We follow Kipper *et al.* (2025) in defining an inner and outer wall radius,  $R_1$  and  $R_2$  respectively, an overall mass,  $M_b$ , and a half-life  $\tau$ . The density for  $R < R_1$  is assumed to be negative and equal to  $-3M_b(t)/4\pi R_1^3$ . The density for  $R_1 \leq R \leq R_2$  is assumed to be equal to  $3M_b(t)/4\pi(R_2^3 - R_1^3)$  to conserve overall disk mass. The total duration of the bubble is  $2\tau$  with time dependence

$$M_b(t, t_o) = M_b \begin{cases} t - t_o & \text{if } 0 < t - t_o < \tau \\ 2\tau - t + t_o & \text{if } \tau < t - t_o < 2\tau \\ 0. & \text{otherwise} \end{cases} \quad (11)$$

The algorithm for super bubbles in EXP is:

1. At every time step, a bubble is generated using a Poisson distribution with rate  $f_b$ . We use the value of  $f_b = 25 \text{ kpc}^{-2} \text{ Gyr}^{-1}$  from Kipper *et al.* (2025) as our fiducial value.
2. When an event occurs, the bubble center is assigned randomly with an exponential disk density distribution with scale length  $a$  and random azimuth  $\phi$  at  $z = 0$ . The bubble is created with time  $t_o = t$  and assigned to the active bubble list.
3. The list of active bubbles is pruned at each time step by removing bubbles with  $t > t_o + 2\tau$ .
4. At each step, the code finds all particles inside any active bubble and computes the force for each bubble on the particle based on the enclosed mass. The force from the bubble is outward from its center.
5. A fixed bubble profile rather than the expanding and contracting model (Kipper *et al.* 2025) will over estimate the effect of the bubbles but compensates for limitations in spatial resolution. As a test, we also explored evaluating the force by projecting the bubble distribution onto the disk expansion basis and allowing the bubbles to change their size in time as proscribed in Kipper *et al.* (2025). The results from this approach are consistent with the direct force evaluation for the time-static bubble profile.

We will see in Section 3.3 that the bubble model for fiducial parameters negligibly affects bar growth compared to the AGN feedback model. For this reason, we abandon further exploration of the details of this bubble model.

#### 2.5. A perturbative simulation

Section 3 shows that application of the AGN feedback model (Sec. 2.4.1) to the full N-body simulation described above leads to a suppression of the bar instability for some ranges of  $\epsilon$  and  $\tau_1$ . To provide explicit dynamical insight, we present an analysis based on the underlying mechanism of the bar instability itself. In particular, Lynden-Bell (1979) elegantly derives a condition for an  $m = 2$  disturbance to grow in a galaxy disk. This idea underpins our understanding of what makes

a bar.<sup>4</sup> The gist of the idea begins with a decomposition of a periodic disturbance into its natural harmonic components in action-angle variables. The existence of this Fourier-type series relies on the pure quasi-periodic nature of orbits in the axisymmetric disk. Each term in the expansion describes the contribution from a particular commensurability:  $l_r\Omega_r + l_\phi\Omega_\phi = 2\Omega_p$  where  $\Omega_r$  and  $\Omega_\phi$  are the radial and azimuthal orbital frequencies, respectively, and  $\Omega_p$  is the bar pattern speed. By restricting one’s attention to the inner Lindblad resonance (ILR) which has  $l_r = -1, l_\phi = 2$ , we get an equation of motion in one degree of freedom. A Taylor series expansion of this equation of motion about the resonant orbit yields Lynden-Bell’s celebrated result: a nascent bar will grow if

$$\mathcal{L} \equiv \frac{\partial^2 H_0}{\partial I_s^2} > 0 \quad (12)$$

where  $H_0$  is the Hamiltonian for the background profile and  $I_s$  is the resonant or *slow* action. For the ILR,  $I_s$  is twice the angular momentum,  $L_z$ . Equation (12) is easily evaluated numerically for any regular system. The marginal growth case for nearly circular orbits occurs for nearly flat but slightly falling rotation curves. Let the maximum angular momentum at fixed guiding-center energy be  $J(E)$ . The general trends are that  $\mathcal{L}$  increases at fixed energy as the relative angular momentum,  $L_z/J(E)$  decreases, and  $\mathcal{L}$  decreases for fixed  $L_z/J(E)$  as the guiding center energy (or radius) increases.

The stochastic processes from Section 2.4 makes analytic predictions challenging. Rather than solve for the system of stochastic ordinary differential equations directly, we use the hybrid numerical perturbation theory framework described in a previous paper (Weinberg and Katz 2007) to obtain a particle system. In essence, the radial motion is much faster than the libration period of the orbit near resonance. The fast motion is therefore adiabatically invariant to changes on the scale of the libration period. This allows us to use the averaging principle to isolate the dynamics controlled by the ILR. This leaves a one-dimensional Hamiltonian described the precession angle,  $w_s$ , and slow action,  $I_s$ , for some effective quadrupole potential describing the full perturbation.

The overall perturbation felt by one phase-averaged particle depends on sum of all other phase-averaged contributions to the effective potential. The density of these phase-averaged particles are quadrupoles that look like dumbbells. The Hamiltonian perturbation theory describes precisely how an ensemble of dumbbells interact. We employ the same mean-field ideas that underlie the BFE N-body methods from EXP (see Section 2.2). Specifically, each dumbbell particle makes a contribution to the mean field of the time-averaged quadrupole potential that is represented by a vector of basis-function coefficients. Appendix B derives this formalism and describes the numerical implementation of the method which we call *BarHMF*.

In the linear limit, the method is a subset of standard matrix response theory used to identify instabilities. It is a subset in the sense that it only includes one or several commensurabilities ( $l_r, l_\phi$ ) while the general

theory includes many. Conversely, this hybrid N-body scheme is itself non-linear: the coupling between phase-averaged particles take the form of coupled non-linear pendula. Therefore, the interaction kernel between all pairs of particles is not limited to linear excitations. For example, the BarHMF simulation demonstrates the expected exponential growth and non-linear saturation of a traditional N-body bar. The dynamics includes trapping effects that are not part of the standard linear response theory. In this sense, we have constructed a particular non-linear analog model that matches linear perturbation theory where it is valid and exhibits many of the features of non-linear bar growth. We will apply the stochastic feedback from Section 2.2 to this idealized bar model to help explain the observed dynamics of the full N-body simulations with AGN feedback.

### 3. RESULTS

We begin in Section 3.1 with a summary demonstration of the consequences to bar formation with a series of 4 runs with successively more AGN central feedback as described in Section 2.4.1. We compare this to bar formation with no feedback in Section 3.2. Section 3.3 shows that bar formation is not sensitive super bubble formation using the model from Section 2.4.2 unless the outflows are unrealistically large and centrally concentrated, much like the AGN model. Later sections describe the sensitivity of the bar interaction to the time scale and amplitude of the AGN feedback process. We end, in Section 3.4.4 with dynamical insight from the BarHMF model.

#### 3.1. AGN feedback: a quick demonstration

A typical central-engine event may be short lived,  $\lesssim 10^4$ – $10^5$  yr (Schawinski *et al.* 2010). This is *sudden* from the orbital viewpoint. However, simulations suggest and observations indicate mass flow events on longer time scales,  $\sim 1$  Myr (Zubovas and Maskeliūnas 2023). Observed bubbles in radio galaxies suggest blowout events with cadence of tens of millions of years (Biava *et al.* 2021). Even longer upper limits follow from considering the duty cycle of observed AGN activity in the Universe assuming that all galaxies have SMBHs. These duty cycles are likely to have been larger at cosmic noon. In summary, estimates of burst frequency vary from 10 Myr to several Gyr. In our stochastic model,  $\tau_1$  is the average time between central events, not the event duration. The key feature is that these burst time scales are comparable to the characteristic dynamical time scales.

For this initial demonstration, we consider four runs of the primary model: the first run has no feedback, the second three fix  $\epsilon = 0.1$  with  $\tau_1 = 20, 40, 80$  Myr from the feedback prescription described in Section 2.4. We explore a larger range for  $\tau_1$  in Section 3.4.2. The results are compared in Figure 1. We adopt  $\tau_2 = \tau_1/2$  in equations (6) and (7) which allows the central disk to recover its lost mass on a time scale shorter than the average interval between outflow events. We have tried other choices, such as  $\tau_2 = \tau_1/4$  and  $\tau_2 = \tau_1$  and the results are qualitatively unchanged. The key dynamical effect is the decorrelation of the orbital precession that is induced by feedback prescription.

The strength of the non-axisymmetric features are nicely described by total power in each azimuthal har-

<sup>4</sup> See the recent paper by Polyachenko and Shukhman (2020) for a description of the mechanism and its history

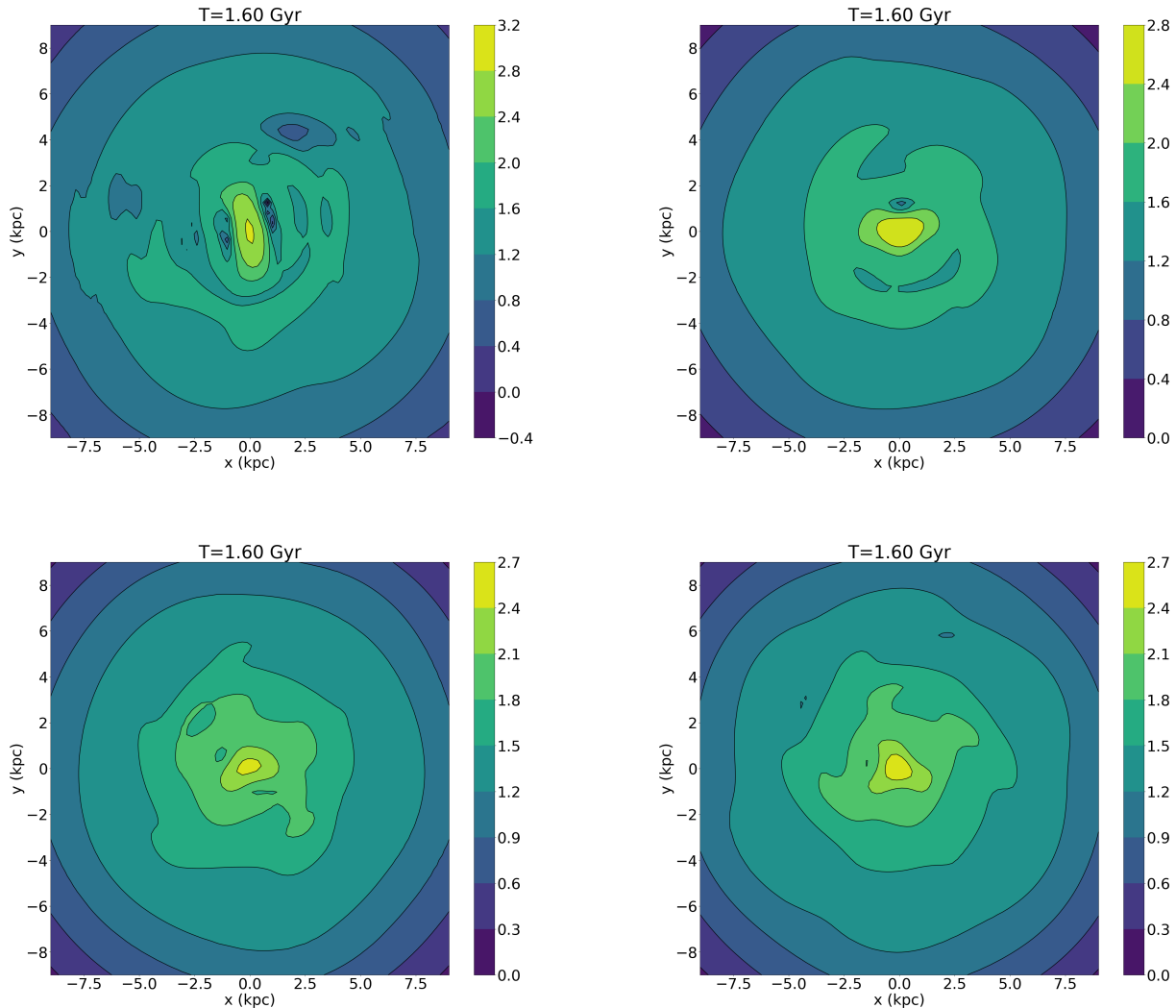


FIG. 1.— The disk surface density at  $T = 1.6$  Gyr. The upper-left panel shows the primary model with no central feedback. The next three panels have central feedback with  $\epsilon = 0.1$  and  $\tau_1 = 20, 40, 80$  Myr and  $\tau_2 = \tau_1/2$ , from left-to-right and top-to-bottom. The density scale is logarithmic in units of  $M_\odot/\text{pc}^2$ .

monic  $m$ . The biorthogonal functions used in the BFE potential solver naturally describe this power. Specifically, the sum of the moduli for all coefficients with a particular value of  $m$  is twice the negative of the total energy in the gravitational field at harmonic order  $m$ ; we define this positive quantity as gravitational power. The square root of this power measures the mean amplitude of the gravitational potential in the BFE (Petersen *et al.* 2022). Figure 2 show the traces of the power for each of the non-axisymmetric orders  $m \in [1, 6]$  for the runs described in Figure 1. In the case without feedback (upper-left panel of Fig. 2), we clearly see coherent signal at all of the even harmonics  $m$  with the amplitude of  $m = 4$  about 0.1 of  $m = 2$ . The  $m = 4$  is responsible for the bar’s *boxiness*. Both dynamics of the bar and the natural modes in the dark-matter halo cause  $m = 1$  distortions. These tend to fluctuate but have similar amplitude to the  $m = 4$  signal. Upon including central feedback, the bar growth is strongly suppressed for all three values of  $\tau_1$ . The  $\tau_1 = 20, 80$  Myr cases reveal some

hint of an  $m = 2$  bar-like feature but comparison with the no feedback run reveals that these are down by an order of magnitude from the no feedback run (upper-left panel). The  $\tau_1 = 40$  Myr case has no obvious bar. The minimum at  $\tau_1 = 40$  Myr is naturally explained by increased coupling between the Markov jump process and the orbital frequencies necessary to support the bar. We will demonstrate this further in Section 3.4.4.

### 3.2. Evolution without feedback

For comparison, we present a brief description of full N-body evolution using the primary model from Section 2.1 *without* any feedback. This provides a reference for comparing the bar growth and evolution to simulations *with* feedback. The salient features of the evolution without feedback are as follows:

1. The growing bar becomes distinct at  $T \approx 600$  Myr.
2. The pattern speed slows quickly during formation as it grows in strength and lengthens.

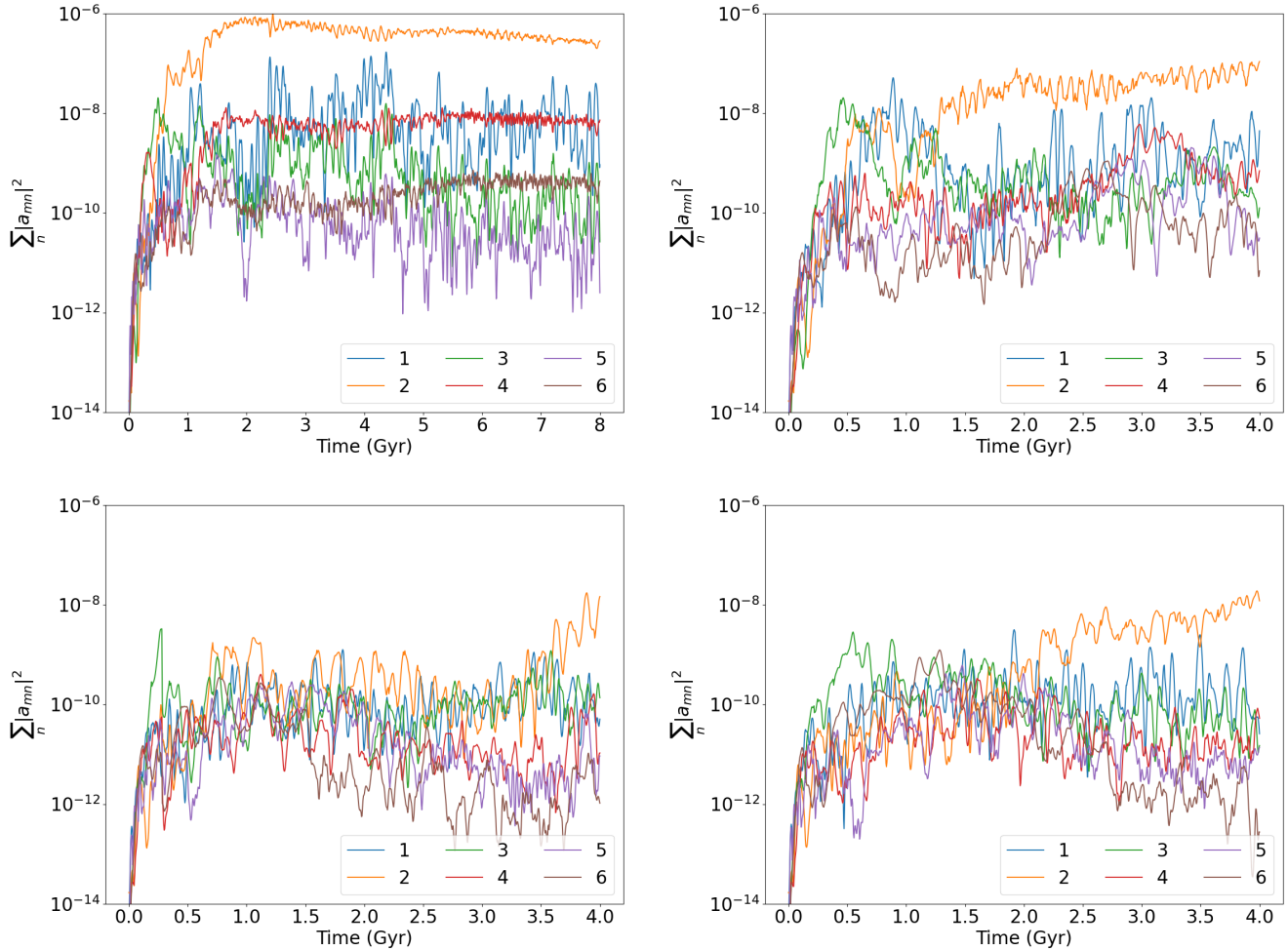


FIG. 2.— The gravitational power for azimuthal harmonics  $m = 1, \dots, 6$  (see inset legends) for each of the four runs from Fig. 1. The power had units of virial energy,  $GM_{vir}^2/R_{vir}$ . The  $m = 5, 6$  harmonics have very little correlated power and are a good indicator of the particle noise floor.

3. The bar reaches an approximate steady-state at  $T \approx 2$  Gyr. The bar pattern speed decays slowly and nearly linearly thereafter.

Figure 3 shows the surface density at the start and at  $T = 1, 2, 4$  Gyr. The first panel shows the initial conditions reconstructed from the BFE. The second panel shows the bar at the of its growth phase. The bar is very slowly evolving in third and fourth panels. The rotation curve for the initial model (Fig. 4) shows the classic linearly rising inner profile that promotes bar growth following the Lynden-Bell condition (eq. 12).

Figure 5 describes the pattern speed,  $\Omega_p$ , which is computed from the complex phase of the first three radial terms in the  $m = 2$  part of the BFE. These first three terms contain 80% of the total  $m = 2$  power and accurately portray the shape and potential of the bar. The rapid change in  $\Omega_p$  for  $600 \text{ Myr} \lesssim T \lesssim 2 \text{ Gyr}$  corresponds to the rapid growth in  $m = 2$  power. In most of this discussion, we will only consider evolution up to  $T = 4$  Gyr given our *cosmic noon* perspective; we show the power in the first panel of Figure 2 and pattern speed in Figure 5 up to  $T = 8$  Gyr for completeness. This run of pattern speed with time compares well with the primary run from Petersen *et al.* (2019) providing a check for the

two-dimensional basis functions described in Section 2.2 and Appendix A. In summary, the orbits driving the bar sheds angular momentum as the bar amplitude grows. These orbits become self-trapped in the quadrupole potential, increasing their eccentricity, lengthening the bar, and decreasing the pattern speed. After the exponential growth phase ceases, the bar continues to grow in mass and length by trapping orbits at the end of the bar and shedding angular momentum to the disk and DM halo. Petersen *et al.* (2019) called this the *secular growth phase*. Without a source new stars or gas, the pattern speed continues to slowly drop and the bar continues to slow growth in mass and length.

### 3.3. Results for SF feedback

Our simulations suggests that AGN feedback creates a global stochastic impulse in the gravitational field that couples to the orbital dynamics of the forming bar. This is corroborated with a dynamical mechanism in Section 3.4.4. However, star-formation outflow is spatially distributed in the disk and each outflow event is individually less massive rather than a centrally concentrated AGN event. In this section, we use the super-bubble model from Section 2.4.2 to explore whether SF outflow has

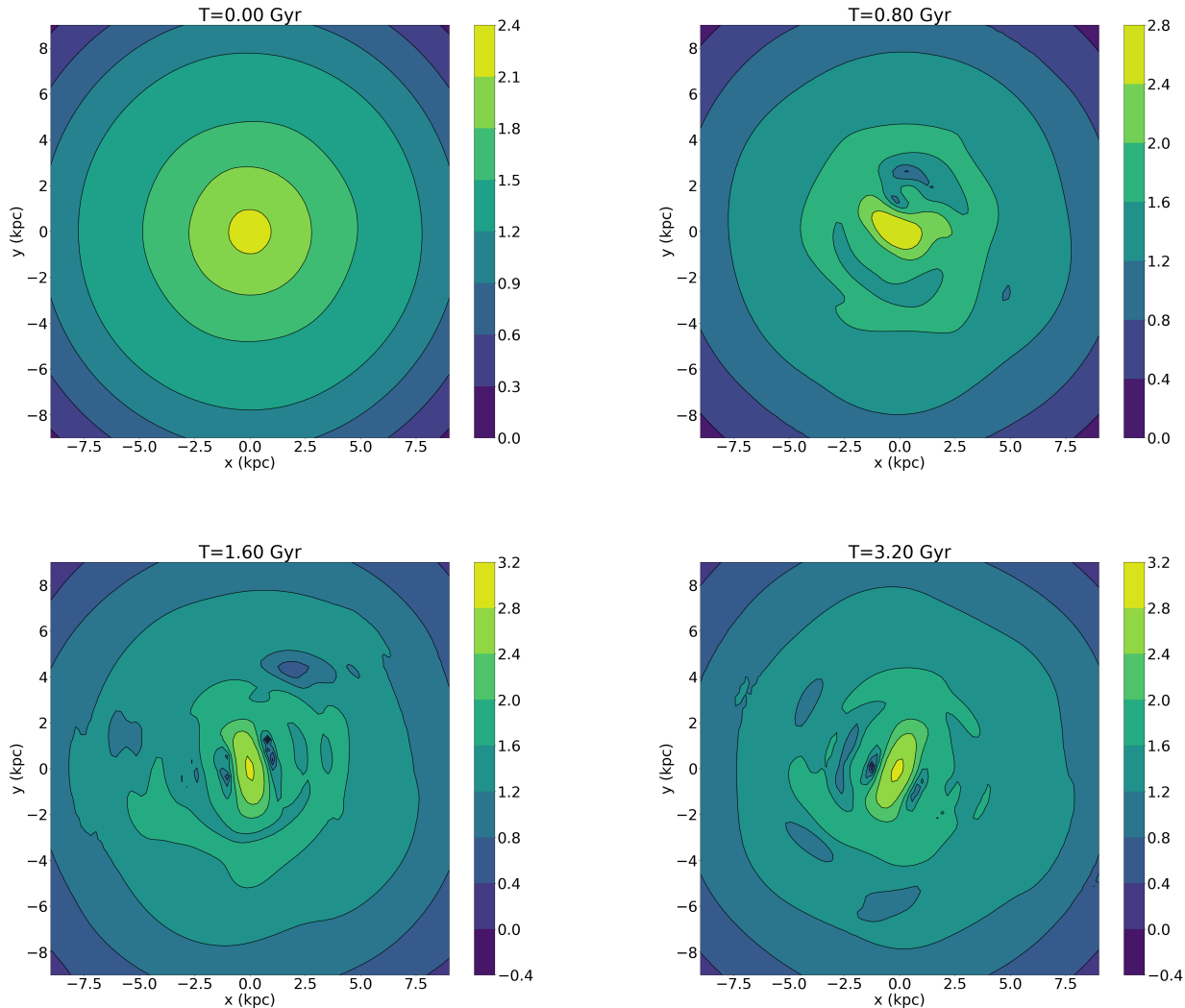


FIG. 3.— The surface density for the *primary* model with no feedback ( $\epsilon = 0$ ) at  $T=0, 0.8, 11.6, 3.2$  Gyr. The bar reaches steady state by  $T = 2$  Gyr. The density scale is logarithmic in units of  $M_{\odot}/\text{pc}^2$ .

a measurable effect on bar growth. This model assumes that super bubbles formed from coalescing individual SN outflows drive outflow events at multiple sites across the disk.

Our fiducial bubble model has  $R_i = 690$  pc,  $R_o = 750$  pc,  $M_b = 1.2 \times 10^4 M_{\odot}$  and half-life  $T = 40$  Myr. The bubble surface density estimate from Kipper *et al.* (2025) for a saturated star burst is  $f_b \approx 25 \text{ kpc}^2 \text{ Gyr}^{-1}$ . We translate this into a rate of bubble production inside of scale length of the disk as described in Section 2.4.2.

A simulation with fiducial parameters has negligible effect on the forming bar. We followed this fiducial simulation with a suite of 54 additional simulations with varying combinations of key parameters in turn. We find that the following changes have negligible effect: (i) doubling the bubble radii  $R_i$  and  $R_o$  for fixed bubble mass  $M_b$ , half-life and rate; (ii) increasing the half-life by a factors of 2, 4, and 8 (iii) increasing the bubble mass  $M_b$  by a factor of 10, 100, and 1000. Conversely, we found that concentrating the bubbles in the center of the galaxy and increasing the mass of the bubbles by factors of 100 or 1000 can slow

or eliminate the bar formation. In other words, when the parameters of the SF model become similar to the AGN model, the same results obtain. In summary, astronomically realistic spatially-distributed SF feedback washes out the correlated signal in the gravitational field fluctuations. While the process provides a background noise, it appears unlikely to generate large enough gravitational potential fluctuations to couple to the dynamics of bar formation.

The mechanism proposed in this paper couples the bar dynamics to large-scale fluctuations in the gravitational potential. However, our bubbles only reach several scale heights above the disk for  $R_o = 750$  pc, so perhaps the lack of a significant effect on bar evolution is not surprising. We have not investigated the work done by galactic fountain generation, and this will be the subject of a future investigation. Meanwhile, the simple AGN feedback mechanism from Section 3.1 also applies to a strong galactic fountain in the inner galaxy. It is the potential fluctuation induced by the mass outflow over a kiloparsec scale, not the loss of the mass as a wind, that causes bar

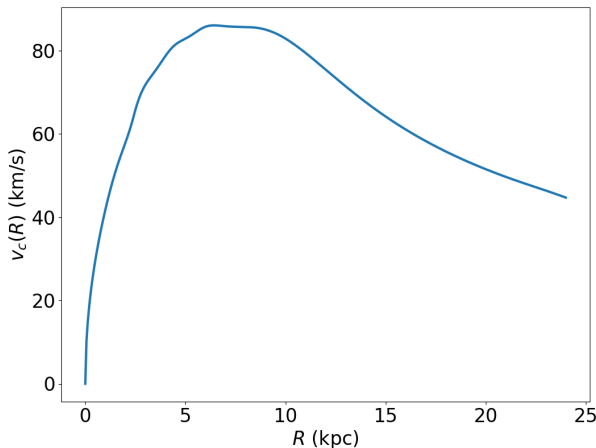


FIG. 4.— The circular velocity curve for the unperturbed halo and disk model described in Section 2.1.2 computed from the radial force in the simulation at  $T = 0$ . The curve is approximately linearly increasing in the first scale length,  $R = 3$  kpc, with a peak at  $R \approx 5$  kpc and a slow decline thereafter.

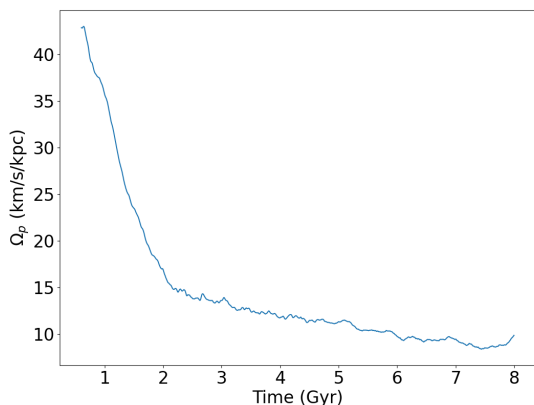


FIG. 5.— Bar pattern speed for the primary run shown from the point of bar assembly onward. The speed decreases over time, indicating suppression or disruption.

### 3.4. Sensitivity to the details of AGN feedback

Having eliminated the SF-driven super bubble feedback model as a plausible influence on bar formation, we return to the AGN feedback model. We quantify the variation of the response with the parameters of the AGN feedback process by considering two distinct scenarios:

1. Fixed  $\tau_1 = 20$  Myr and varying amplitude of the mass loss,  $\epsilon$  in Section 3.4.1.
2. Fixed  $\epsilon = 0.3$  and varying the value of  $\tau_1$  in Section 3.4.2.

While the duration of the AGN energy injection may be shorter than  $\tau_1$ , and a wind crossing time is  $\sim 1$  Myr, the relevant time scale for dynamical coupling is the response of the system to the sudden change in the gravitational potential induced by the outflow. This occurs on the dynamical time scales for the surrounding galaxy. These timescales are tens to hundreds of Myr.

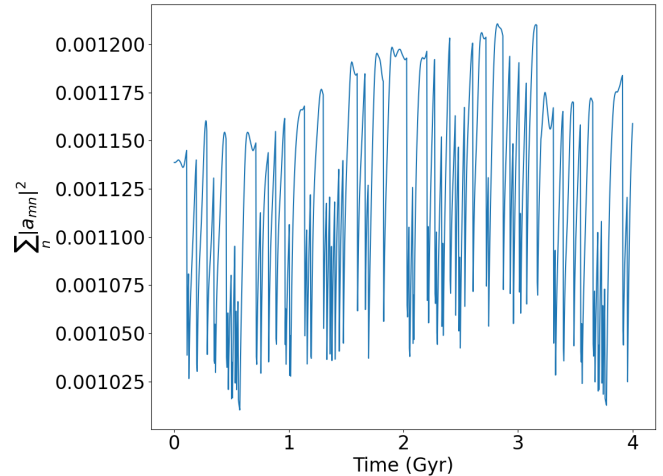


FIG. 6.— The run of  $m = 0$  power for the  $\epsilon = 0.1$ ,  $\tau_1 = 40$  Myr simulation to illustrate the fluctuation in the gravitational power induced by star formation events. See Fig. 2 for an illustration of the non-axisymmetric power in the same simulation.

#### 3.4.1. Comparison of frequencies

We fix  $\epsilon = 0.1$ ; equation (8) implies that the mass that temporarily leaves the disk per outflow event is 1.4% of the total disk mass ( $7 \times 10^7 M_\odot$ ). This is consistent with observed estimates (Santoro *et al.* 2020) over 10 Myr.

The  $m = 0$  component represents most of the gravitational power in the disk and is not shown in Figure 2 to emphasize the non-axisymmetric components. We illustrate the effect of star-formation feedback on the gravitational power of the  $m = 0$  component alone in Figure 6 for the  $\tau_1 = 40$  Myr run. The value  $\epsilon = 0.1$  affects the total gravitational potential energy of the disk at a level of approximately 0.8%.

#### 3.4.2. Comparison of amplitudes

Next, we fix  $\tau_1 = 20$  Myr and examine the variance with  $\epsilon \in [0.1, 0.3, 0.5]$ . Equation (8) implies that the mass lost per outflow event for these values of  $\epsilon$  are 1%, 4%, and 7%, respectively. These results are summarized and compared with results from previous section in Figure 7. This figure shows the ratio of the BFE amplitudes (root power) at  $m = 2$  for the varied values of  $\tau_1$  and  $\epsilon$  with those from the primary model without feedback at  $T = 1, 2, 4$  Gyr. As expected, the lower panel shows that larger values of mass loss,  $\epsilon$ , lead to smaller amplitude ratios at all times. The upper panel summarizes the results from the previous section with an extended range of  $\tau_1$  from 10–500 Myr: the largest damage is done to the bar instability for  $\tau_1 \approx 50$  Myr. This time interval is close to the characteristic orbital time for inner bar orbits. As  $\tau_1$  increases, the amplitude ratio increases. However, even for large value of  $\tau_1 = 500$  Myr, the bar amplitude is suppressed by a factor of two. To index the amplitude ratio to bar morphology, the second panel from Figure 1 is an amplitude ratio of 0.23. The next two panels are ratios of 0.13 and 0.03. The 0.23 case (second panel) is typical of a weak bar and ratios below  $\sim 0.2$  (third and fourth panels) are not bar-like.

We chose the value of  $\epsilon = 0.1$  used in Section 3.4.2 to be close to the critical threshold for significant suppression

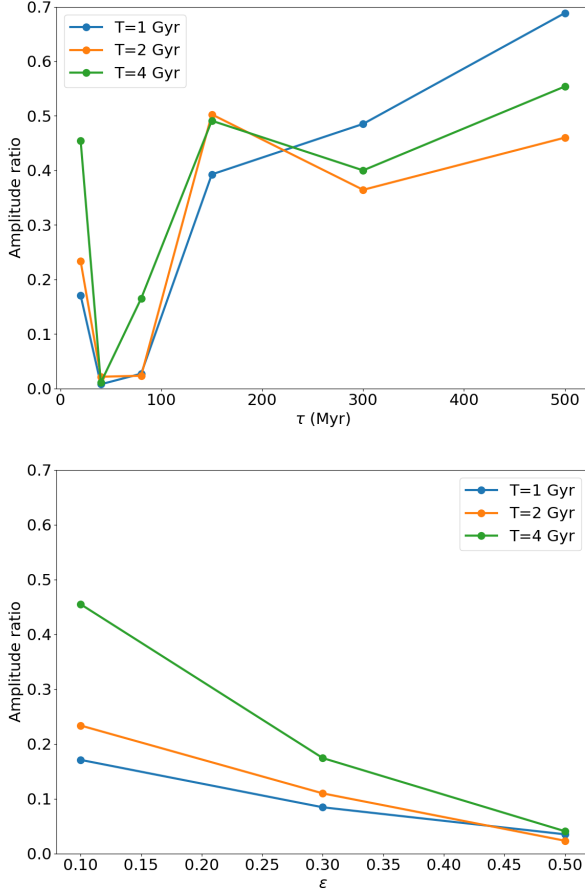


FIG. 7.— The ratio of the  $m = 2$  amplitudes at  $T = 1, 2, 4$  Gyr in simulations with AGN feedback to the  $m = 2$  amplitude from the primary simulation without feedback. Top: constant value of  $\epsilon = 0.1$  with values of  $\tau_1$  along the x-axis. Bottom: constant value of  $\tau_1 = 20$  Myr with values of  $\epsilon$  along the x-axis.

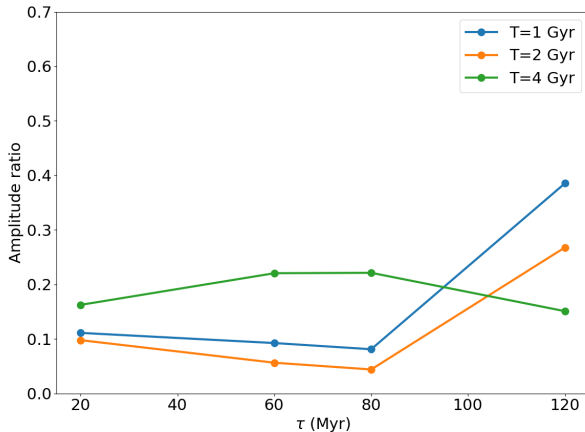


FIG. 8.— As in the top panel of Fig. 7 but for  $\epsilon = 0.3$ . Here, the suppression ratios are smaller overall with less variation in  $\tau_1$ .

of the bar formation. For the larger value of  $\epsilon = 0.3$ , the amplitude ratios for various values of  $\tau_1$  are shown in Figure 8. The overall values of the suppression ratios are smaller, as expected, and the sensitivity to value of  $\tau_1$  are much weaker.

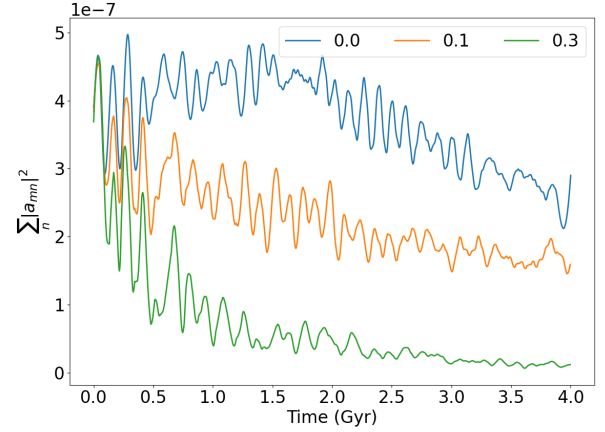


FIG. 9.— The primary model is evolved without AGN feedback until  $T = 2$  Gyr and then subjected to feedback. This figure shows the  $m = 2$  power after feedback commences for various amplitudes,  $\epsilon$ . The run with  $\epsilon = 0.0$  has no feedback, for comparison. A model with  $\epsilon = 0.1$  reduces the bar amplitude by a factor of 2 and the model with  $\epsilon = 0.3$  eliminates the bar after 2 Gyr.

### 3.4.3. The effect of feedback on a preexisting bar

Bar formation in an otherwise quiescent galaxy could be the source of gas advection that induces a central star burst. We ask whether our Markov-process AGN feedback model can be used to destroy a preexisting bar? We begin with the phase space from the primary N-body simulation without AGN feedback at  $T = 2$  Gyr shown in Figure 3. We then apply the stochastic model with two different feedback strengths,  $\epsilon = 0.1, 0.3$ . We set  $\tau_1 = 20$  Myr with  $\tau_2 = \tau_1/2$  as in previous cases. These two cases are compared with the no feedback ( $\epsilon = 0$ ) case in Figure 9. For  $\epsilon = 0.1$ , the feedback diminishes the bar amplitude by a factor of 2; the bar reaches a new steady-state amplitude in approximately 4 Gyr. For  $\epsilon = 0.3$ , the bar is destroyed after 2 Gyr. Some  $m = 2$  power remains in the form of an oval distortion at larger radii than the original bar.

In summary, the AGN feedback model can be used to destroy an existing bar. More feedback amplitude is required to destroy it than to prevent it owing to the extra self-gravity in the bar itself. We suggest exploring this scenario using existing suites of cosmological galaxy formation simulations that include feedback. Barred galaxies are ubiquitous in simulations of isolated galaxies at the present epoch although it is clear observationally that not all disk galaxies have bars. It has been argued that central mass concentrations may be sufficient to destroy bars although there is some numerical evidence to the contrary (Athanasoula 2005). The feedback model proposed here provides another possible bar destruction mechanism.

### 3.4.4. Insight from perturbation theory

Section 2.5 and Appendix B describes a simulation method tailored to the dynamics of Lynden-Bell's mechanism specifically. In essence, each simulation particle contributes its part to the ensemble action-angle expansion of gravitational potential restricted to the same commensurate term considered by Lynden-Bell (1979). Given that this model is a cousin of the classical cosine HMF ring model (Antoni and Ruffo 1995) specialized to

the interaction implied by the Lynden-Bell mechanism, we find the term BarHMF to be an apt descriptor. Although the model employs an interaction potential from linear theory, it is a non-linear model. Indeed, Appendix B demonstrates that many of the basic results of bar formation and growth from full N-body simulations are found in the BarHMF model. For example, the BarHMF model reproduces the non-linear saturation of the bar amplitude with a growth rate proportional to disk mass.

The perturbation scheme outlined in Section 2.4 is applied to the BarHMF simulation as follows. The axisymmetric component of the gravitational potential is represented by a spherical monopole for computational convenience. In other words, the disk does not have its own  $m = 0$  self gravity but does have  $m = 2$  self gravity. The Markov-process AGN feedback model changes the central mass through equation (6) and causes fluctuations in the monopole that affect the BarHMF dynamics. A feedback event implies in an overall decrease in central mass according to Step 2 in the algorithm from Section 2.4. This mass change is applied suddenly as in the full N-body simulation. This increases the energy of the BarHMF particles by  $\delta E = GM_d \epsilon / (\mu \lambda a)$  where  $\mu$  parametrizes the change in gravitational potential caused by the feedback-induced mass loss. We choose  $r_g \equiv \mu \lambda a$  to be the gravitational radius of the monopole contribution of the total gravitational energy from change in disk mass inside of  $\lambda a$ . For a spherical model,  $r_g$  is approximately 0.4 times the half-mass radius of the disk mass enclosed by  $\lambda a$  (Binney and Tremaine 2008) and determines  $\mu$ . This approximation most likely underestimates the effect on the disk for a given  $\epsilon$  but is consistent with the assumptions in our BarHMF application.

The main difference between the AGN model for BarHMF and the full EXP model is that both the change in energy and recovery time is instantaneous for BarHMF and only the change in energy is instantaneous for the EXP model. This is consistent with the time averaging implicit in the BarHMF contribution to the interaction potential: the decay time  $\tau_2$  from equation (7) is shorter than the orbital time and therefore instantaneous in the time-averaged Hamiltonian context.

The BarHMF particles interact with each other (see Appendix B). For particles with the same action values, the coupling depends on the precession angles of their apsides relative to the bar position angle in some frame rotating at pattern speed  $\Omega_p$ . The precession frequency is small compared to the mean orbital frequency for orbits comprising the bar. For example, the *perfect* bar supporting trajectory has zero precession frequency with respect to the bar major axis. For a slightly *imperfect* bar supporting trajectory, the angle of apsides will precess slowly relative to the bar pattern. For this reason, the action conjugate to the precession angle is called the *slow* action and is proportional to the angular momentum. The precession angle itself is called the *slow* angle. There is a second degree of freedom whose frequency is proportional to the orbital frequencies and therefore faster than the precession frequency. The BarHMF particles result from an average over this *fast* degree of freedom leaving only one active *slow* degree-of-freedom.

Without any external perturbations, the fast action is conserved for all time. A mass-loss event causes a sudden change in energy and radial action. This fluctua-

tion is axisymmetric, conserving the angular momentum of stellar trajectories; therefore the *slow* action remains unchanged. However, the *fast* action is a linear combination of the radial action and angular momentum. The fast action changes as result of the energy causing a jump in radial action. If these jumps in fast action are sufficiently large, a BarHMF particle which had been librating about the about the bar position can find itself precessing away from the bar. This causes the bar to grow more slowly, decay, or not grow at all.

We illustrate the dynamics in a simple case of two BarHMF particles at one disk scale length orbiting in the truncated NFW-like model (eq. 2). Each trajectory feels a change in energy from a mass-loss event every  $\tau_1 = 20$  Myr. Each event removes  $2 \times 10^8 M_\odot$  from the inner 20% of the disk scale length (600 pc for the Milky Way). We assume that this quickly cools back on the disk maintaining a steady state potential punctuated by instantaneous changes in the radial action. The mass is not required to escape the gravitational potential of the galaxy to have affect; it only needs to be pushed out to a few kpc. Figure 10 shows two BarHMF runs that differ only in their initial  $\Delta w_s$ : the first of these runs begins with  $\Delta w_s = 0.02$  (or  $\approx 1^\circ$  shown in blue) and the second begins with  $\Delta w_s = 1.0$  (or  $\approx 57^\circ$  shown in orange). The first run undergoes significant jumps in  $\Delta w_s$  but remains in libration. The jumps in the second with larger libration amplitude are enough to push the trajectory from libration into rotation. The dashed curves depict the same trajectories without perturbation and can be compared to the two-particle BarHMF runs from Appendix B in Figure 13.

Figures 11 shows the BarHMF model described in Appendix B for the NFW-like background model that is generally bar promoting. Each of these simulations has  $N = 1000$  particles<sup>5</sup> and uses  $\tau_1 = 20$  Myr. The legend describes the mass loss per AGN event in solar masses scaled to Milky Way units for familiarity. For no feedback at all, the bar exponential grows in approximately 2 Gyr before leveling off into a steady state. Recall that there is no coupling between the bar and disk or halo so the bar can not slow. For  $4 \times 10^7 M_\odot$  per event, the bar grows more slowly then levels off and begins to decay. The overall saturation amplitude is a factor of 5 smaller than with no feedback at all. For a mass loss of  $2 \times 10^8 M_\odot$  per event, the bar grows but very slowly, reaching only 10% of its saturation amplitude in Figure 2 at  $T = 4$  Gyr. For larger mass loss events, the bar can not grow at all.

The thresholds in  $\epsilon$  appear to be larger here than for the full simulation. This may have a number of causes. First, this may be an artifact of the spherical background model and the gravitational radius approximation. The work done on the spherical potential from the feedback is likely to be relatively smaller in effect for the spherical monopole than for the flat axisymmetric disk. Secondly, the initial actions are chosen for a fixed eccentricity with guiding centers in a narrow ring as described in Appendix B. The resulting dynamics will differ from the full simu-

<sup>5</sup> BarHMF particles are spatially distributed and this specialized simulation require fewer particles to reach convergence. Conversely, these simulations are more expensive per particle than a traditional N-body See Appendix B for more discussion.

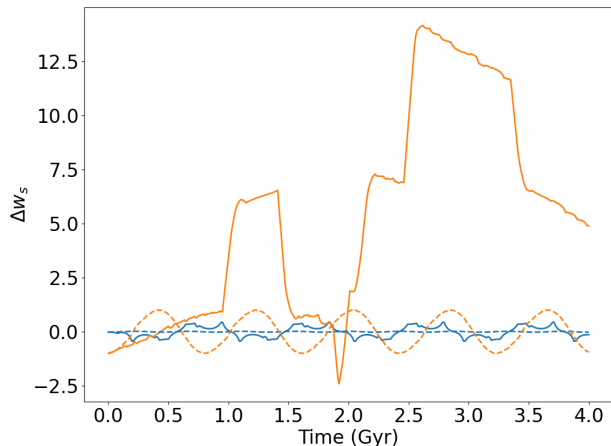


FIG. 10.— Change in relative precession angle,  $\Delta w_s$ , for a two-particle BarHMF simulation with AGN feedback. The mass-loss events, which occur every 20 million years push  $2 \times 10^8 M_\odot$  into the inner halo. We assume that this quickly cools back on the disk maintaining a steady state. The sudden change in gravitational potential changes the fast action for each trajectory. The two runs differ only in their initial  $\Delta w_s$  with 0.02 rad (blue) and 1.0 rad (orange). The dashed curves show the run of  $\Delta w_s$  without feedback.

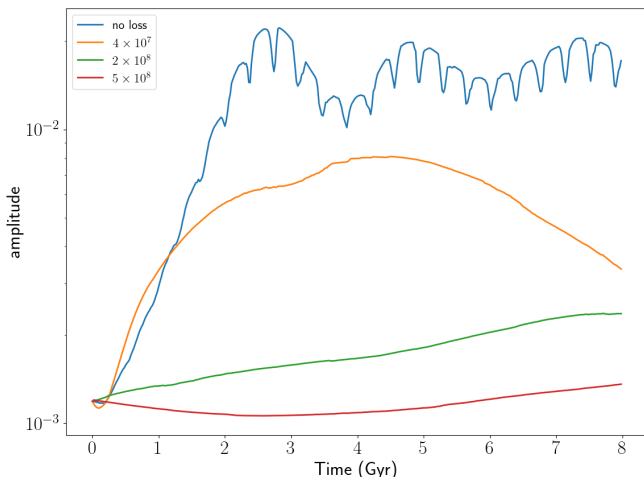


FIG. 11.— Bar growth as a function of mass loss per event (in  $M_\odot$ ) for the BarHMF in Milky Way units of  $10^{12} M_\odot$  for easy comparison. The event frequency is  $\tau = 20$  Myr.

lation that has a disk with an astronomically motivated exponential distribution. We have chosen the total mass of the BarHMF particles to approximate the mass of the exponential disk between pericenter and apocenter, but we do not expect a one-to-one correspondence with full N-body simulations. Nonetheless, the qualitative trends are similar which suggest that the BarHMF dynamics represents the main features of the underlying mechanism.

#### 4. CONCLUSIONS

We investigate the dynamical importance of feedback-induced gravitational fluctuations on the bar instability using a Markov jump-process model; intervals between

feedback events are random draws from a Poisson distribution. We began with a full N-body simulation of a galactic disk in a live dark-matter halo with a mass typical of a disk at  $z \sim 2.5$  which is roughly a factor of four lower than at  $z = 0$ . Our primary, unperturbed model forms a stable bar in approximately 1 Gyr. We model the gravitational influence of AGN feedback by perturbing that simulation with a stochastic mass-loss process which removes a small fraction  $\epsilon$  of mass in the inner disk at a characteristic time  $\tau_1$ . The mass is lost from the inner 2/3 of the disk scale length or 2 kpc in Milky-Way units, causing a gravitational fluctuation in energy. The lost mass is assumed to resettle on the disk at another characteristic time  $\tau_2$ . We choose  $\tau_2 \lesssim \tau_1$  typical of the AGN event frequency: between 10 and 100 Myr. We parametrize the mass-loss strength as the fraction of the disk mass in the inner 2/3 of the disk scale length in the resulting outflow. The amplitude of the mass loss ranges from 1% to 7% of the total disk mass. The process itself is designed to capture the temporal features of gravitational fluctuations from feedback; we intend for ranges in amplitude,  $\epsilon$ , and time scales,  $\tau_1$  and  $\tau_2$ , (Fig. 7) to be compared to detailed physical models.

We also explored a star-formation (SF) model inspired by the super-bubble model from Kipper *et al.* (2025). We find that the stochastic feedback from SF outflows in super bubbles does not provide sufficient correlated dynamical fluctuations to couple to the bar formation mechanism. However, this model does *not* include the work done by a galactic fountain on the potential. The two models together suggest that approximately 1% disk-mass fluctuations in the inner galaxy are key to coupling feedback to stellar bar suppression. Specifically, the AGN feedback model also applies to strong SF-driven outflows.

To gain physical insight into the dynamical nature of the coupling between feedback and the bar instability, we developed a novel one-degree-of-freedom simulation based on the classical bar instability from linear perturbation theory (Lynden-Bell 1979). Each particle in the simulation interacts with the bulk of particle ensemble through the quadrupole force exerted near resonance. In other words, each particle is dumbbell-shaped in space with two actions characterizing its radial extend and spread. The one degree of freedom is its azimuthal orientation. This specialized simulation reproduces all of the major features the bar instability in the full N-body simulation including non-linear saturation of the exponential growth (see Appendix B).

We may use this model to understand the dynamics of coupling. In the absence of feedback, only the net angular momentum of stellar orbits change through resonant interaction. A particular linear combination of the radial action and angular momentum remains invariant. The bar begins with the chance positional alignment of some dumbbell orientations. Their collective gravity cause more dumbbells to align, driving an exponential instability. However, the fluctuations in the gravitational potential induced by star-formation process affects the previously invariants, by changing the radial action. These fluctuations disturb the libration of particles in the quadrupole of the bulk, slowing or eliminating the bar instability depending on the strength of the feed-

back.

A final caveat: please note that this study considers a single, isolated galaxy model with an exponential disk and a dark-matter halo (see Section 2.1 for details). The disk mass of  $5 \times 10^9 M_\odot$  and lack of bulge or spheroid component are chosen to produce a bar within 2 Gyr without feedback. This is consistent with our goal of investigating the dynamics that couples stochastic events to the bar instability. For example, a more concentrated model might slow bar formation and change the rate of pattern speed evolution.

The key findings are as follows:

1. Mass-loss fractions of  $\epsilon \geq 0.1$  in the inner few kiloparsecs of a disk are enough to dramatically affect the bar formation. These result in bar amplitude that are at most 50% of the unperturbed case.
2. We demonstrate that fluctuations in the gravitational potential of the inner galaxy couple to the radial action of orbits in the bar instability. These fluctuations reduce or eliminate the bar instability, consistent with the results of the full N-body simulation. This simple model provides a way of predicting the importance of AGN feedback to disk instabilities.
3. We tested both AGN-inspired and SF-inspired feedback models. The mass loss is central in the AGN model and disk-distributed for SF-inspired model. We find that the central feedback typical of AGN mass outflows provides sufficient correlated change in the gravitational potential to affect the bar growth mechanism. Conversely, the SF model does not provide sufficient temporally correlated change to couple. Strong, central SF-induced fluctuations in the field may occur during massive bursts but are not typical of those typically observed at lower redshift.
4. The cadence of feedback events matters. The bar amplitude is reduced by an order of magnitude (and some cases suppressed altogether) if  $\tau_1$  roughly matches the typical orbital period. This makes good dynamical sense. If disk orbits respond to the self-gravity of a quadrupole by precessing towards the potential well of the quadrupole, the bar amplitude will grow. However, if this precession is disrupted by changes in the underlying potential, this growth is reduced or eliminated.
5. For large amplitude mass loss events, e.g. closer to our upper limit of 7% mass changes per event, the amplitude of bar growth is suppressed independent of  $\tau_1$ .

6. The bars that do form in the presence of significant feedback-induced fluctuations are poorly organized in a qualitative sense. They tend to shed mass and lose stability as star-formation events continue.

Our overall focus is the mechanism that connects the stochastic nature of galaxy feedback mechanisms with the smooth orbital motion of classical galaxy dynamics. As in dynamics generally, the key important quantities are frequencies. A stochastic process can be characterized by its autocorrelation function, and here, the process is Poisson, with a characteristic frequency  $\sim 1/\tau_1$ . The coincidence  $\tau_1 \sim \tau_{dyn}$  suggests the possibility of interesting coupling. The importance of this coupling to the overall dynamics of the bar instability depends on the details and requires explicit calculation. To that end, we provide evidence for its magnitude and importance by a combination of direct N-body simulation and a idealized simulation restricted to the dynamics of bar instability specifically. The similarity of the behavior in the two calculations suggests that we have successfully described the mechanism.

We emphasize that the details of the feedback process have been greatly simplified in this study. For example, we have assumed pure axisymmetric central fluctuations in our AGN feedback model, ignoring non-axisymmetric dependence. Rather, we explored the two important parameters of the simplest possible stochastic model that excites gravitational fluctuations—an amplitude and characteristic frequency—and provide predictions for range of those quantities necessary to have impact on the bar formation. Motivated by rough estimates from more detailed observational and theoretical studies, we find that range of these parameters overlap predicted ranges of AGN-driven outflow and recurrence. The expected diversity of galaxy formation conditions and SMBH masses suggest that the coupling between feedback and bar formation will not be binary; some systems may still be able to easily form bars at early epochs and others not. Moreover, we have demonstrated that strong feedback coupling may be capable of eroding and even destroying a bar after formation.

MDW thanks Julien Devriendt and Christophe Pichon whose enthusiasm motivated me to attack this problem. MDW is grateful to Mike Petersen and Chris Hamilton for discussions and to Carrie Filion, Chris Hamilton, Mike Petersen and Christophe Pichon for helpful comments on the manuscript. We also thank the anonymous referees who provided helpful criticism that helped tighten the conclusions. This research was supported in part by grant NSF PHY-1748958 to the Kavli Institute for Theoretical Physics (KITP).

#### REFERENCES

- J. A. L. Aguerri, J. Méndez-Abreu, and E. M. Corsini, *A&A* **495**, 491 (2009), arXiv:0901.2346 [astro-ph.GA].
- F. Hohl, *ApJ* **168**, 343 (1971).
- J. P. Ostriker and P. J. E. Peebles, *ApJ* **186**, 467 (1973).
- D. Lynden-Bell and A. J. Kalnajs, *MNRAS* **157**, 1 (1972).
- S. Tremaine and M. D. Weinberg, *MNRAS* **209**, 729 (1984).
- E. Athanassoula, *MNRAS* **341**, 1179 (2003), astro-ph/0302519.
- Y. Guo, S. Jogee, S. L. Finkelstein, Z. Chen, E. Wise, M. B. Bagley, G. Barro, S. Wuyts, D. D. Kocevski, J. S. Kartaltepe, E. J. McGrath, H. C. Ferguson, B. Mobasher, M. Giavalisco, R. A. Lucas, J. A. Zavala, J. M. Lotz, N. A. Grogin, M. Huertas-Company, J. Vega-Ferrero, N. P. Hathi, P. A. Haro, M. Dickinson, A. M. Koekemoer, C. Papovich, N. Pirzkal, L. Y. A. Yung, B. E. Backhaus, E. F. Bell, A. Calabrò, N. J. Cleri, R. T. Coogan, M. C. Cooper, L. Costantin, D. Croton, K. Davis, A. Dekel, M. Franco, J. P. Gardner, B. W. Holwerda, T. A. Hutchison, V. Pandya, P. G. Pérez-González, S. Ravindranath, C. Rose, J. R. Trump, A. de la Vega, and W. Wang, *The Astrophysical Journal Letters* **945**, L10 (2023).

- J. Binney and S. Tremaine, *Galactic Dynamics: (Second Edition) (Princeton Series in Astrophysics)* (Princeton University Press, 2008).
- M. S. Petersen, M. D. Weinberg, and N. Katz, MNRAS **490**, 3616 (2019), arXiv:1903.02566 [astro-ph.GA].
- M. S. Petersen, M. D. Weinberg, and N. Katz, MNRAS **500**, 838 (2021), arXiv:1902.05081 [astro-ph.GA].
- D. Ceverino and A. Klypin, The Astrophysical Journal **695**, 292 (2009).
- J. Kormendy and L. C. Ho, ARA&A **51**, 511 (2013), arXiv:1304.7762 [astro-ph.CO].
- T. M. Heckman, L. Armus, and G. K. Miley, ApJS **74**, 833 (1990).
- P. F. Hopkins and L. Hernquist, MNRAS **402**, 985 (2010), arXiv:0910.4582 [astro-ph.CO].
- F. Combes, S. García-Burillo, J. Braine, E. Schinnerer, F. Walter, and L. Colina, A&A **550**, A41 (2013), arXiv:1209.3665 [astro-ph.CO].
- F. Combes, Frontiers in Astronomy and Space Sciences **4**, 10 (2017), arXiv:1707.09621 [astro-ph.GA].
- P. Madau and M. Dickinson, ARA&A **52**, 415 (2014), arXiv:1403.0007 [astro-ph.CO].
- S. Veilleux, G. Cecil, and J. Bland-Hawthorn, ARA&A **43**, 769 (2005), arXiv:astro-ph/0504435 [astro-ph].
- A. King and K. Pounds, ARA&A **53**, 115 (2015), arXiv:1503.05206 [astro-ph.GA].
- D. Zhang, Galaxies **6**, 114 (2018), arXiv:1811.00558 [astro-ph.GA].
- F. Governato, B. Willman, L. Mayer, A. Brooks, G. Stinson, O. Valenzuela, J. Wadsley, and T. Quinn, MNRAS **374**, 1479 (2007), arXiv:astro-ph/0602351 [astro-ph].
- T. Zana, P. R. Capelo, M. Dotoli, L. Mayer, A. Lupi, F. Haardt, S. Bonoli, and S. Shen, MNRAS **488**, 1864 (2019), arXiv:1810.07701 [astro-ph.GA].
- G. Ogiya and M. Mori, ApJ **793**, 46 (2014), arXiv:1206.5412 [astro-ph.CO].
- R. Kipper, I. Vurm, A. N. Triantafyllaki, P. Tenjes, and E. Tempel, A&A **693**, A206 (2025), arXiv:2404.18086 [astro-ph.GA].
- D. Lynden-Bell, MNRAS **187**, 101 (1979).
- P. H. Chavanis, J. Vatteville, and F. Bouchet, European Physical Journal B **46**, 61 (2005), arXiv:cond-mat/0408117 [cond-mat.stat-mech].
- J. F. Navarro, C. S. Frenk, and S. D. M. White, ApJ **490**, 493 (1997), arXiv:astro-ph/9611107 [astro-ph].
- B. Diemer and A. V. Kravtsov, ApJ **799**, 108 (2015), arXiv:1407.4730 [astro-ph.CO].
- W. Hu, R. Barkana, and A. Gruzinov, Phys. Rev. Lett. **85**, 1158 (2000), arXiv:astro-ph/0003365 [astro-ph].
- L. Hui, J. P. Ostriker, S. Tremaine, and E. Witten, Phys. Rev. D **95**, 043541 (2017), arXiv:1610.08297 [astro-ph.CO].
- E. V. Polyachenko, P. Berczik, and A. Just, MNRAS **462**, 3727 (2016), arXiv:1601.06115.
- J. A. Sellwood, ApJ **819**, 92 (2016), arXiv:1601.03406.
- E. Athanassoula, R. E. G. Machado, and S. A. Rodionov, MNRAS **429**, 1949 (2013), arXiv:1211.6754 [astro-ph.CO].
- M. Aumer, J. Binney, and R. Schönrich, MNRAS **459**, 3326 (2016), arXiv:1604.00191.
- A. Collier, I. Shlosman, and C. Heller, MNRAS **476**, 1331 (2018a), arXiv:1712.02802.
- A. Collier, I. Shlosman, and C. Heller, ArXiv e-prints (2018b), arXiv:1811.00033.
- M. Clutton-Brock, Ap&SS **16**, 101 (1972).
- M. Clutton-Brock, Ap&SS **23**, 55 (1973).
- L. Hernquist and J. P. Ostriker, ApJ **386**, 375 (1992).
- M. D. Weinberg, AJ **117**, 629 (1999), arXiv:astro-ph/9805357 [astro-ph].
- M. S. Petersen, M. D. Weinberg, and N. Katz, MNRAS **510**, 6201 (2022), arXiv:2104.14577 [astro-ph.GA].
- M. S. Petersen and M. D. Weinberg, Journal of Open Source Software **10**, 7302 (2025).
- G. E. Romero, A. L. Müller, and M. Roth, A&A **616**, A57 (2018), arXiv:1801.06483 [astro-ph.HE].
- N. Yadav, D. Mukherjee, P. Sharma, and B. B. Nath, MNRAS **465**, 1720 (2017), arXiv:1603.00815 [astro-ph.HE].
- C.-G. Kim and E. C. Ostriker, ApJ **846**, 133 (2017), arXiv:1612.03918 [astro-ph.GA].
- E. V. Polyachenko and I. G. Shukhman, MNRAS **498**, 3368 (2020), arXiv:2007.05187 [astro-ph.GA].
- M. D. Weinberg and N. Katz, MNRAS **375**, 425 (2007), arXiv:astro-ph/0508166 [astro-ph].
- K. Schawinski, D. A. Evans, S. Virani, C. M. Urry, W. C. Keel, P. Natarajan, C. J. Lintott, A. Manning, P. Coppi, S. Kaviraj, S. P. Bamford, G. I. G. Józsa, M. Garrett, H. van Arkel, P. Gay, and L. Fortson, ApJ **724**, L30 (2010), arXiv:1011.0427 [astro-ph.CO].
- K. Zubovas and G. Maskeliūnas, MNRAS **524**, 4819 (2023), arXiv:2306.00518 [astro-ph.GA].
- N. Biava, M. Brienza, A. Bonafede, M. Gitti, E. Bonnassieux, J. Harwood, A. C. Edge, C. J. Riseley, and A. Vantyghem, A&A **650**, A170 (2021), arXiv:2104.08294 [astro-ph.HE].
- F. Santoro, C. Tadhunter, D. Baron, R. Morganti, and J. Holt, A&A **644**, A54 (2020), arXiv:2009.11175 [astro-ph.GA].
- E. Athanassoula, Monthly Notices of the Royal Astronomical Society **358**, 1477 (2005).
- M. Antoni and S. Ruffo, Phys. Rev. E **52**, 2361 (1995).
- T. A. Zang, *The Stability of a Model Galaxy*, Ph.D. thesis, Massachusetts Institute of Technology (1976).
- L. Yu, M. Huang, M. Chen, W. Chen, W. Huang, and Z. Zhu, Optics Letters **23**, 409 (1998).
- M. Guizar-Sicairos and J. C. Gutiérrez-Vega, Journal of the Optical Society of America A **21**, 53 (2004).
- G. N. Watson, *A Treatise on the Theory of Bessel Functions*, second edition ed. (Cambridge University Press, 1941).
- A. Toomre, ApJ **138**, 385 (1963).
- M. D. Weinberg, ApJ **368**, 66 (1991).
- H. Goldstein, C. P. Poole, and J. Safko, *Classical Mechanics*, 3rd ed. (Addison-Wesley, 2002).
- H. Yoshida, Physics Letters A **150**, 262 (1990).
- J. Sanz-Serna and M. Calvo, *Numerical Hamiltonian Problem*, Dover Books on Mathematics (Dover, 2018).
- M. Tao, Phys. Rev. E **94**, 043303 (2016).
- B. W. Silverman, *Density Estimation for Statistics and Data Analysis* (Chapman and Hall, London, 1986).
- G. Contopoulos, A&A **201**, 44 (1988).
- B. V. Chirikov, Phys. Rep. **52**, 263 (1979).
- T. Manos and E. Athanassoula, MNRAS **415**, 629 (2011), arXiv:1102.1157 [astro-ph.GA]

## APPENDIX

## A. TWO-DIMENSIONAL DISK BASES

The latest version of EXP (Petersen and Weinberg 2025) includes two-dimensional cylindrical disk bases with three-dimensional gravitational fields. This allows for gravitational couples between two- and three-dimensional components. These bases are used for the simulations in Section 3 that include the coupling to the dark-matter halo. For completeness, this section describes the construction and computation of the two-dimensional cylindrical bases as used by EXP.

We construct two-dimensional polar bases using the same empirical orthogonal function (EOF) technique used to compute the three dimensional cylindrical basis (Petersen *et al.* 2022). In essence, we compute the Gram matrix whose entries are the inner product of an input basis weighted by the density of the desired equilibrium profile. The new

basis functions are the input basis weighted by each of the eigenvectors of the Gram matrix. The construction provides a basis *conditioned* by the target equilibrium galaxy profile. The user has the choice of two possible two-dimensional input bases:

1. The cylindrical Bessel functions of the first kind,  $J_m(\alpha_{m,n}R/R_{max})$  where  $\alpha_{m,n}$  is the  $n^{\text{th}}$  root of  $J_m$  and  $R_{max}$  is an outer boundary. Thus, orthogonality is defined over a finite domain by construction.
2. The Clutton-Brock two-dimensional basis (Clutton-Brock 1972) which orthogonal over the semi-infinite domain.

The user then chooses a conditioning density. Currently, these are the exponential disk, the Kuzmin (Toomre) disk, the finite Mestel disk (Binney and Tremaine 2008), the tapered Mestel or Zang disk (Zang 1976). The code was written to allow for a user-defined density function and this will be available in a future release of EXP.

The coupling between the two-dimensional disk and other three-dimensional components (e.g. a dark-matter halo or a bulge) requires evaluating the gravitational potential and its gradient everywhere in space. The three-dimensional gravitational potential is not *automatically* computed by the two-dimensional recursion relations that define the biorthogonal functions but can be evaluated by Hankel transform. Numerically, this can be done very accurately over a finite domain with the quasi-discrete Hankel transformation (QDHT, Yu *et al.* 1998; Guizar-Sicairos and Gutiérrez-Vega 2004). The QDHT algorithm exploits special properties of the Bessel functions and is best suited for finite density profiles whose two-dimensional gravitational potential are well-described using the cylindrical Bessel basis. This is automatically true for the EOF bases derived from the cylindrical Bessel functions. For this reason, the Clutton-Brock basis should only be used for EOF basis construction for applications where the three-dimensional gravitational potential is not needed.

The in-plane density, potential and force fields are one-dimensional functions for each azimuthal order  $m$  and radial order  $n$ . EXP tables the EOF basis solutions on a fine grid and evaluates these with linear interpolation. This is numerically efficient and accurate. The potential and force fields for  $|z| > 0$  require two-dimensional tables. Similarly, EXP finely-grids these functions in two-dimensional tables and evaluates them with bilinear interpolation.

The remainder of this section describes the implementation of the two-dimensional basis. We begin in Section A.1 with a summary of the QDHT algorithm followed by its application to the Hankel transform that defines two-dimensional biorthogonal basis functions in Section A.2. The complete algorithm is presented in Section A.3 followed by a discussion of the pros and cons of this approach in Section A.4.

#### A.1. A brief description of the QDHT algorithm

The development here follows Yu *et al.* (1998). The continuous Hankel transform pair is

$$\begin{aligned} g(k) &= \int_0^\infty dr r f(r) J_\nu(kr), \\ f(r) &= \int_0^\infty dk k g(k) J_\nu(kr), \end{aligned} \quad (\text{A1})$$

where  $J_\nu$  is the Bessel function of the first kind of integer order  $\nu$ . The discrete Hankel transform may be obtained from equation (A1) by imposing

$$\begin{aligned} g(k) &= 0 & \text{for } k > K, \\ f(r) &= 0 & \text{for } r > R. \end{aligned}$$

Using this condition in equations (A1) yields:

$$\begin{aligned} g(k) &= \int_0^R dr r f(r) J_\nu(kr), \\ f(r) &= \int_0^K dk k g(k) J_\nu(kr). \end{aligned} \quad (\text{A2})$$

We can now use the usual Fourier-Bessel expansion (Watson 1941) to evaluate  $f(r)$  as follows:

$$f(r) = \sum_{m=1}^{\infty} C_{\nu m} J_\nu\left(a_{\nu m} \frac{r}{R}\right) \quad (\text{A3})$$

for  $0 \leq r \leq R$  where

$$C_{\nu m} = \frac{2}{R^2 J_{\nu+1}^2(a_{\nu m})} \int_0^R dr r f(r) J_\nu\left(\alpha_{\nu m} \frac{r}{R}\right) \quad (\text{A4})$$

and  $\alpha_{\nu m}$  is the  $m^{\text{th}}$  root of  $J_\nu$ . Equation (A4) is a direct application of the well-known orthogonality relation for Bessel functions of the first kind. By inspection, it is clear that:

$$C_{\nu m} = \frac{2}{R^2 J_{\nu+1}^2(a_{\nu m})} g\left(\frac{\alpha_{\nu m}}{R}\right). \quad (\text{A5})$$

The continuous transform in equations (A2) becomes a discrete transform by choosing the evaluation points for  $r$  and  $k$  as:

$$\begin{aligned} r_j &= \frac{\alpha_{\nu j}}{K} \\ k_j &= \frac{\alpha_{\nu j}}{R}. \end{aligned} \quad (\text{A6})$$

Substituting into equation (A3) and using equation (A5), we get

$$f\left(\frac{\alpha_{\nu n}}{V}\right) = \sum_{m=1}^{\infty} \frac{2}{R^2 J_{\nu+1}^2(a_{\nu m})} g\left(\frac{\alpha_{\nu m}}{R}\right) J_{\nu}\left(\frac{\alpha_{\nu m} \alpha_{\nu n}}{RK}\right) \quad (\text{A7})$$

and by symmetry

$$g\left(\frac{\alpha_{\nu m}}{R}\right) = \sum_{n=1}^{\infty} \frac{2}{K^2 J_{\nu+1}^2(a_{\nu n})} f\left(\frac{\alpha_{\nu n}}{K}\right) J_{\nu}\left(\frac{\alpha_{\nu m} \alpha_{\nu n}}{RK}\right). \quad (\text{A8})$$

Truncating the upper limit of sum of the indices  $m$  and  $n$  to some value  $N$  in equations (A7) and (A8) yields the discrete Hankel transform. The symmetry in these two equations can be made manifest by defining further the two vectors with elements

$$\begin{aligned} F_i &= \frac{f(\alpha_{\nu i}/K)R}{J_{\nu+1}(\alpha_{\nu i})} \\ G_i &= \frac{g(\alpha_{\nu i}/R)K}{J_{\nu+1}(\alpha_{\nu i})} \end{aligned} \quad (\text{A9})$$

and the matrix with elements

$$T_{ij} = \frac{2}{RK J_{\nu+1}(a_{\nu i}) J_{\nu+1}(a_{\nu j})} J_{\nu}\left(\frac{\alpha_{\nu m} \alpha_{\nu n}}{RK}\right). \quad (\text{A10})$$

Then, the discrete Hankel transform may be written in matrix notation as

$$\begin{aligned} \mathbf{G} &= \mathbf{T} \cdot \mathbf{F}, \\ \mathbf{F} &= \mathbf{T} \cdot \mathbf{G}. \end{aligned} \quad (\text{A11})$$

The transform is very accurate numerically, typically one part in  $10^8$  in algorithm tests, when the target function is well-represented by a Bessel expansion,

### A.2. Construction of a biorthogonal basis

Armed with the finite Hankel transform and an algorithm for its evaluation, we derive a two-dimensional biorthogonal basis using the eigenfunctions of the Laplacian described in Toomre (1963) and clearly summarized in §2.6.2 of Binney and Tremaine (2008). Specifically, gravitational potential functions in the form

$$\Phi_m(r, \phi; k) = e^{im\phi} J_m(kr) \quad (\text{A12})$$

have the surface density

$$\Sigma_m(r, \phi; k) = \frac{k}{2\pi G} e^{im\phi} J_m(kr) \quad (\text{A13})$$

Using the notation from the previous section, let

$$\begin{aligned} \Phi_{mj}(r, \phi) &= D_{mj} e^{im\phi} J_m(\alpha_{mj}r/R), \\ \Sigma_{mj}(r, \phi) &= (-1)^m \frac{\alpha_{mj}}{2\pi RG} D_{mj} e^{im\phi} J_m(\alpha_{mj}r/R), \end{aligned} \quad (\text{A14})$$

where  $D_{mj}$  is a normalization. Using the standard properties of Bessel functions, we may write:

$$\begin{aligned} (\Phi_{m'j}, \Sigma_{mk}) &= \int_0^{2\pi} d\phi \int_0^R dr r \Phi_{m'j}^*(r) \Sigma_{mk}(r) \\ &= D_{mj} D_{mk} \frac{\alpha_{mj}}{RG} \int_0^R dr r J_m(\alpha_{mj}r/R) J_m(\alpha_{mk}r/R) \\ &= \frac{\alpha_{mj}}{2RG} J_m^2(\alpha_{mj+1}) D_{mj}^2 \delta_{m'm} \delta_{jk}. \end{aligned} \quad (\text{A15})$$

Setting equation (A15) equal to one defines the normalizing coefficient  $D_{mj}$  in equations (A14). Finally, we can use the EOF conditioning procedure described above and in Petersen *et al.* (2022) to obtain a new biorthogonal basis that best fits a desired equilibrium density model. This new basis is related to equations (A14) by a linear transformation.

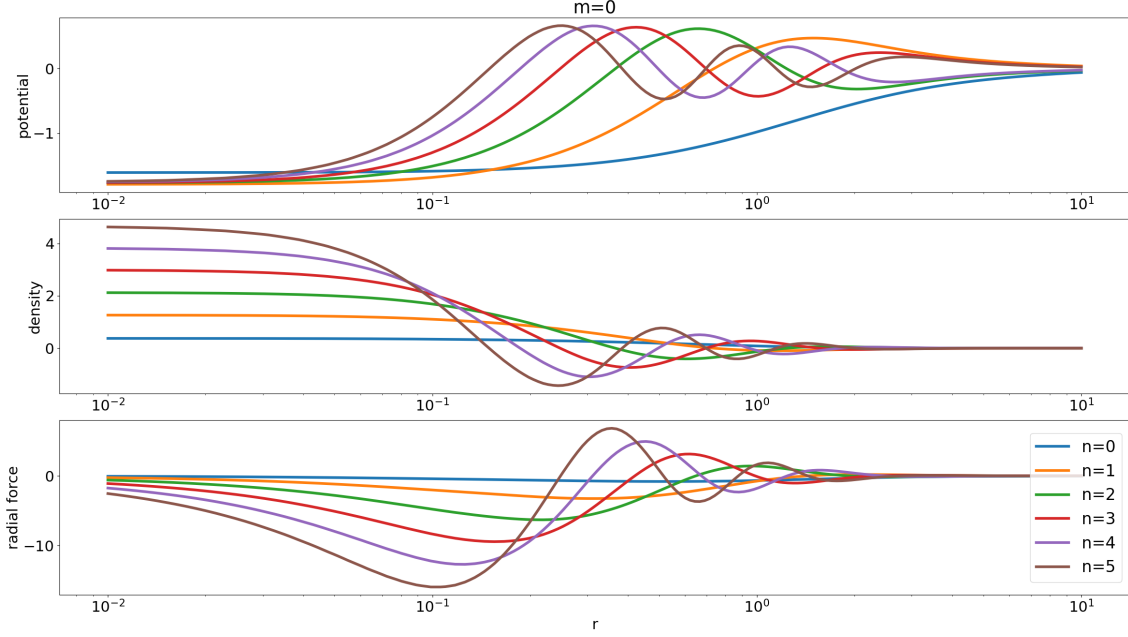


FIG. 12.— Biorthogonal  $m = 0$  basis functions for the two-dimensional exponential disk with scale length  $a = 1$ . The color key describes the radial index,  $n$ . The  $n = 0$  basis function has no radial nodes. The  $n = 1$  function has one radial node. Each successive function has one more radial node. The exponential density conditioning leads to nodes distributed like the cumulative mass by construction.

In the application needed here, we want to describe the gravitational potential for three dimensional space. We may use Toomre (1963) to do this. For razor-thin disk with surface density  $\Sigma(r, \phi)$ , the gravitational potential is:

$$\Phi(r, \phi, z) = \sum_{m=-\infty}^{\infty} \int_0^{\infty} dk S_m(k) J_m(kr) e^{im\phi - k|z|} \quad (\text{A16})$$

where

$$\Sigma_m(r) \equiv \frac{1}{2\pi} \int_0^{2\pi} d\phi e^{-im\phi} \Sigma(r, \phi) \quad (\text{A17})$$

and

$$S_m(k) = -2\pi G \int_0^{\infty} dr r J_m(kr) \Sigma_m(r) \quad (\text{A18})$$

If we use a surface density based on the Bessel basis from equations (A14), the integrals are accurately computed from the discrete Hankel transform described in the previous section.

### A.3. Algorithm

Putting this development together, we may summarize the computation of the gravitational potential in  $R, \phi, z$  as follows:

1. Choose the edge of the radial domain:  $R$ .
2. Choose a Bessel expansion order:  $N$ .
3. Choose  $RK = \alpha_{m, N+1}$  to minimize the error matrix as described in Yu *et al.* (1998). This defines the value  $K = \alpha_{m, N+1}/R$ .
4. The evaluation knots are then as in equation (A6) for  $j \in [1, \dots, N]$ .
5. Compute the matrix  $\mathbf{T}$  from equation (A10).
6. Compute the vector  $\mathbf{F}$  for the surface density  $\Sigma_m$  to get the discrete Hankel transform:  $\mathbf{G} = \mathbf{T} \cdot \mathbf{F}$ .
7. Compute the potential integrand:

$$\mathbf{K} = \left\{ \frac{e^{-|\mathbf{k}|z}}{\mathbf{k}} \right\} \otimes \mathbf{G}$$

or equivalently  $K_j = -\exp(-k_j|z|)G_j/k_j$ .

8. Compute the inverse discrete Hankel transform to get:

$$\Phi = \mathbf{T} \cdot \mathbf{K}$$

9. Finally, the evaluation of  $\Phi$  at an arbitrary value of  $r$  may be accurately performed using equation (A8) as an interpolation formula.

#### A.4. Discussion

The main advantages of the strategy outlined in this section for numerically evaluating the three-dimensional gravitational potential for a razor-thin disk are:

1. One can condition the biorthogonal Bessel-function basis on any well-behaved target density, similar to the three-dimensional case.
2. The Hankel transform necessary to obtain the off-plane potential is very accurate.

The disadvantages of this approach are:

1. It works well *only* for a basis with a finite extent. The Hankel transformation for an infinite domain is numerically challenging. We have had good success using QDHT, so we recommend the finite basis for this reason. This restriction to a finite-domain is not a problem in practice for simulations whose implementations are numerically finite.
2. The Bessel functions are asymptotically oscillatory and the truncation to order  $N$  will leave their oscillatory imprint at larger radii. Again, this is not a problem for simulations where the larger disk radii are not dynamically important.

While the code implemented in EXP allows the conditioning on the 2d Clutton-Brock basis, the computation of the vertical potential is less accurate for the same computational work using QDHT. This could be improved by truncating the basis and implementing Neumann boundary conditions with appropriate outgoing eigenfunctions. That has not been done here. Another solution might be an asymptotic numerical evaluation of the Hankel transform at large cylindrical radii patched onto a brute force quadrature at small radii. At this point, we recommend the Bessel basis for accuracy, especially for coupling the disk response another three-dimensional component such as a bulge or halo. If only the two-dimensional in-plane evaluations are needed (e.g. a two-dimensional disk in a fixed halo), both basis choices will be equally good.

## B. HAMILTONIAN PERTURBATION THEORY

The bar growth and instability in a two-dimensional disk is mediated by the inner Lindblad resonance (ILR) as described in Lynden-Bell (1979). In essence, Lynden-Bell describes bar growth by determining the conditions for a test-particle orbit to precess towards the a quadrupole disturbance presented by the mean-field of all other orbits in the vicinity of the test particle (see Section 2.5 for more discussion).

To help understand the N-body dynamics described in Section 3, we use the same Hamiltonian perturbation theory to derive a constrained N-body simulation that excerpts the ILR interaction from the perturbation theory and treats it as the fundamental interaction between phase-averaged particles. The new simulation method is itself non-linear while reproducing the linear perturbation theory in the linear limit. The numerical method parallels the N-body method described in Section 2.2: it represents the mean gravitational field of the particle ensemble interacting near the ILR using a biorthogonal expansion. This development generalizes the well-known *Hamiltonian Mean Field* or cosine model (Chavanis *et al.* 2005) in philosophy, if not physical detail. The cosine model assumes that the potential of each pairwise interaction of particles  $i, j$  on a ring with position angle  $\theta$  is  $\cos(\theta_i - \theta_j)$ . The model below is a cosine model whose coefficients depend on actions that exactly represent the orbit-averaged contributions to the mean field. The pairwise interactions are replaced with the interaction of each particle with the mean contribution of all particles. For brevity and with apologies for a small abuse of terminology, we will call this the *BarHMF* model. We will see in Section B.4 that the BarHMF model captures many of the interesting linear and non-linear aspects of bar growth and instability that we see in the full N-body simulations. This correspondence allows us to use this model to help explain the N-body simulations in Section 3.

### B.1. Perturbation theory

The linear response theory has been described in many places and this development parallels Tremaine and Weinberg (1984) and Weinberg (1991). Our goal here is to present enough of the mathematical derivation to motivate the hybrid N-body solution. We consider a non-axisymmetric gravitational potential:

$$U_p(\mathbf{r}, t) = \sum_m U_m(r) e^{im(\phi - \Omega_{pm}t)}. \quad (\text{B1})$$

with a well-defined pattern speed,  $\Omega_{pm}$ , for each azimuthal harmonic,  $m$ . For comparison with the results in Section 3, we restrict ourselves to the single  $m = 2$  polar harmonic. We assume a regular axisymmetric background potential.

The background potential is independent of the particle dynamics. The orbital dynamics may be fully expressed in action-angle coordinates. We will denote the angle and action vectors by  $(\mathbf{w}, \mathbf{I})$  where index 1 (2) is the radial (azimuthal) degree of freedom. To make explicit correspondence with the flat disk considered in this paper, we have  $I_1 = I_r$  (radial action) and  $I_2 = J = L_z$  (angular momentum) with  $l_1 = l_r$  and  $l_2 = l_\phi$ . This allows us to expand any function of phase space as Fourier expansion:

$$U(\mathbf{w}, \mathbf{I}, t) = \sum_m \sum_{l'_1=-\infty}^{\infty} \sum_{l'_2=-m}^m W_{l'_1 m}(\mathbf{I}) e^{i(l'_1 \cdot \mathbf{w} - m \Omega_{p2} t)}, \quad (\text{B2})$$

where  $\mathbf{l} = (l_1, l_2)$  and

$$W_{l m}(\mathbf{I}) = \frac{1}{(2\pi)^2} \oint dw_1 dw_2 e^{-i(l \cdot \mathbf{w} - m \Omega_{p2} t)} U(\mathbf{w}, \mathbf{I}, t). \quad (\text{B3})$$

If we now specialize this to equation (B1) with the assumption of a fixed axisymmetric background and  $m = 2$  only, we find

$$W_{l_2}(\mathbf{I}) = \delta_{l_2 2} \frac{1}{2\pi} \oint dw_1 e^{-i[l_1 w_1 + l_2 f(w_1)]} U_2(r(\mathbf{w}, \mathbf{I})) \quad (\text{B4})$$

where  $w_2 = \phi + f(w_1)$ . The function  $f(w_1)$  represents the shift of azimuth from that of the guiding center owing to the radial motion (Tremaine and Weinberg 1984). This is a direct consequence of conservation of angular momentum. Equation (B4) is one-dimensional periodic quadrature that can be numerically computed to very high accuracy with little overhead.

The radial function  $U_2(r)$  in equation (B1) is arbitrary. Next, we will assume that  $U_2(r)$  can be expanded in the biorthogonal basis as described in Appendix A:  $\Phi_{mj}$  for  $j \in [0, n_{max}]$ . This yields

$$U_2(r) = \sum_{j=0}^{n_{max}-1} a_j \Phi_{mj}(r) \quad (\text{B5})$$

where  $a_j$  are expansion coefficients. We may explicitly compute and table the angle transforms for each  $j$

$$W_{l_2}^j = \delta_{l_2 2} \frac{1}{2\pi} \oint dw_1 e^{-i[l_1 w_1 + l_2 f(w_1)]} \Phi_{2j}(r(\mathbf{w}, \mathbf{I})) \quad (\text{B6})$$

over a grid in  $I_1, I_2$  for numerical evaluation.

### B.2. Averaging

We now apply the averaging principle. The idea is simple: near a particular resonance, the libration angle defined as  $\mathbf{l} \cdot \mathbf{w} - \Omega_{p2} t$  is very slowly changing relative to either component of  $\mathbf{w}$ . This allows us to make a simple canonical transformation to a linear combination of angles and actions where one of the new coordinates is this libration angle by construction. Let the new angles and actions be  $\mathcal{W} = (w_s, w_f)$  and  $\mathcal{I} = (I_s, I_f)$ , respectively. Let us choose the Type 2 generating function (Goldstein *et al.* 2002)

$$F_2(\mathcal{I}, \mathbf{w}) = (\mathbf{l} \cdot \mathbf{w} - \Omega_{p2} t) I_s + w_1 I_f. \quad (\text{B7})$$

Simple calculation immediately shows that  $w_s = \mathbf{l} \cdot \mathbf{w} - \Omega_{p2} t$ ,  $w_f = w_1$ ,  $I_1 = l_1 I_s + I_f$  and  $I_2 = l_2 I_s$ . The new Hamiltonian is  $\mathcal{H} = H - 2\Omega_{p2} I_s$ . There is some arbitrariness in the choice of  $F_2$  but the important feature is that  $w_s$  changes slowly compared to the change in  $w_f$ .

Armed with this development, we average equation (B2) over a time interval  $T$  chosen so that  $2\pi/\Omega_1 \ll T \ll 2\pi/(\mathbf{l} \cdot \boldsymbol{\Omega} - 2\Omega_{p2})$ . By construction, all terms in the sum are rapidly varying in this interval except for the one with  $l'_1 = l_1$  and  $l'_2 = l_2$ . Our perturbed Hamiltonian for the averaged system reduces to a single term:

$$H_1(\mathbf{w}, \mathbf{I}) = W_{l_2}(\mathbf{I}) e^{i w_s}. \quad (\text{B8})$$

Expressed in the biorthogonal basis, this may be written as

$$H_1(\mathbf{w}, \mathbf{I}) = \sum_{j=0}^{n_{max}-1} a_j W_{l_2}^j(\mathbf{I}) e^{i w_s}. \quad (\text{B9})$$

Now, let us take some ensemble of  $N$  particle trajectories. At any particular time  $t$ , a single trajectory indexed by  $k$  contributes

$$\begin{aligned} \delta a_j &= \int d\mathbf{r} \delta(\mathbf{r} - \mathbf{r}_k(t)) \Phi_{mj}(r) e^{-im(\phi - \Omega_{p2} t)} \\ &= \int dr \delta(r - r_k(t)) \Phi_{mj}(r) \int d\phi \delta(\phi - \phi_k(t)) e^{-im(\phi - \Omega_{p2} t)} \end{aligned} \quad (\text{B10})$$

to the coefficient  $a_j$  where  $\delta(\cdot)$  is the Dirac delta function. The averaging principle requires an average of the fast action to get the *slow* contribution. The contribution of a single averaged trajectory indexed by  $k$  to  $a_j$  is

$$\begin{aligned} a_j^k &= \frac{1}{2\pi} \oint dw_f \delta a_j \\ &= \frac{\delta_{l_2, m}}{2\pi} \oint dw_f \Phi_{l_2 j}(r(\mathbf{w}, \mathbf{I})) e^{-il_2(w_2 - f(w_1) - m\Omega_{p2}t)} \\ &= e^{-i(l_1 w_1 + l_2 w_2 - m\Omega_{p2}t)} \frac{\delta_{l_2, m}}{2\pi} \oint dw_1 \Phi_{l_2 j}(r(\mathbf{w}, \mathbf{I})) e^{i(l_1 w_1 + l_2 f(w_1))} \\ &= e^{-iw_s} W_{12}^{j*}(\mathbf{I}), \end{aligned} \tag{B11}$$

where we used  $w_2 = \phi + f(w_1)$  in the second equality, explicitly held  $w_s$  fixed during the average of  $w_f = w_1$  in the third equality, and identified  $W_{12}^j(\mathbf{I})$  from equation (B6). The values of  $w_s$  and  $\mathbf{I}$  are those of trajectory  $k$ .

The Hamilton equations for a particular phase trajectory then become:

$$\dot{w}_s = \frac{\partial H}{\partial I_s} = \frac{\partial \mathcal{H}}{\partial I_s} + \frac{\partial H_1}{\partial I_s} = \mathbf{l} \cdot \boldsymbol{\Omega} - 2\Omega_{p2} + e^{iw_s} \sum_{j=0}^{n_{max}-1} a_j \frac{\partial W_{12}^j(\mathbf{I})}{\partial I_s}, \tag{B12}$$

$$\dot{I}_s = -\frac{\partial H}{\partial w_s} = -ie^{iw_s} \sum_{j=0}^{n_{max}-1} a_j W_{12}^j(\mathbf{I}). \tag{B13}$$

The first term in equation (B12) is the unperturbed frequency of the slow motion. This frequency vanishes at the resonance. The final terms in each of equations (B12) and (B13) describe the perturbation from the quadrupole component contributed by each particle. This is a pendulum equation where the pendulum arm has a general dependence on the action of the particle.

### B.3. The hybrid simulation method

We begin by adopting the biorthogonal basis from Appendix A that matches the simulations in Section 3. We represent the axisymmetric background potential by the spherical halo model from Section 2.1.1 for computational convenience and simplicity; using a combined disk, bulge, dark-matter halo background field is straightforward but not necessary for this demonstration. The particle motion remains planar by construction. Then, we tabulate the values of  $W_{12}^k(\mathbf{I})$  on a two-dimensional grid in  $\mathbf{I}$ . The actions of the simulation particles can be chosen according to some distribution. For studies here, we distribute guiding centers in a smooth distribution in a particular annulus. The initial distribution of  $w_s$  is chosen in one of two ways: (1) random in  $[0, 2\pi]$  or (2) uniformly spaced in  $[0, 2\pi]$  with an specific excess in a small interval of  $(-\epsilon, \epsilon)$  to seed the perturbation. For Case 1, the small variations from uniform are sufficient to seed an instability for a bar-unstable system. For Case 2 without an excess, a uniform distribution will remain close to equilibrium for an unreasonably long time. In other words, this choice relies on numerical noise to produce an asymmetry that grows. This motivates adding a small deviation to seed a disturbance.

Our simulation particles only contribute their quadrupole component from a single  $\mathbf{I}$  term in equation (B2) to the gravitational field. Each particle begins with a mass, actions  $I_f$  and  $I_s$  and slow angle  $w_s$ . Without external influences, the fast action  $I_f$  is fixed throughout. However, under the influence of the Markov jump process described in Section 2.4, both  $I_f$  and  $I_s$  can change as described in Section 3.4.4. The fast action,  $I_f$ , changes result from the gravitational fluctuations and the slow action,  $I_s$ , changes as a result of the quadrupole field. Assume that we have  $N$  particles of mass  $m_k$  distributed as described in the previous paragraph. The mean-field potential is determined by summing the contributions of each particle to the  $n_{max}$  numerically-determined coefficients  $\hat{a}_j$ :

$$\hat{a}_j = \sum_{k=1}^N m_k a_j^k = \sum_{k=1}^N m_k e^{-iw_k} W_{12}^{j*}(\mathbf{I}_k). \tag{B14}$$

The averaging smooths out each particle's spatial contribution from pericentre to apocentre. This results in a faster convergence with particle number  $N$  and radial order  $n_{max}$  than a traditional N-body code. If we define  $J(E)$  as the maximum value of orbital angular momentum,  $J$ , at particular energy  $E$ , a converged series is obtained for  $n_{max} = 6$  for modestly eccentric orbits with  $J/J(E) = 0.8$ .

The simulation proceeds by solving  $2N$  first-order ODE defined by equations (B12) and (B13) for  $w_s$  and  $I_s$  respectively. Without any external perturbations, the fast actions  $I_f$  are constant for the entire simulation. However, the background values for  $\Omega_1(\mathbf{I})$ ,  $\Omega_2(\mathbf{I})$ ,  $W_{12}^k(\mathbf{I})$  and other phase-space quantities needed by equations (B12) and (B13) are naturally tabulated in  $I_1$  and  $I_2$  or  $E$  and  $L = I_2$ . Thus, any changes in  $I_s$  imply both changes  $E$  and  $L$ . New values are computed using bilinear interpolation on precomputed grids of size  $400 \times 400$ .

Unfortunately, this Hamiltonian flow is not explicitly separable which complicates the choice of an ODE solver. Recall that a Hamiltonian system is *separable* if the Hamiltonian can be written as  $H(\mathbf{q}, \mathbf{p}) = K(\mathbf{p}) + V(\mathbf{q})$  where  $K$  and  $V$  most often correspond to the kinetic and potential functions, and is non-separable otherwise. A separable

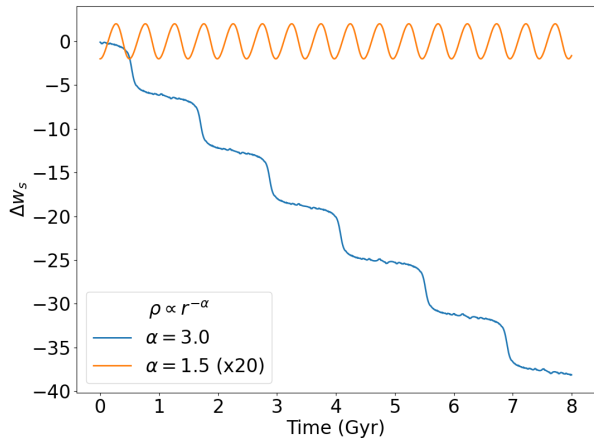


FIG. 13.— Difference in slow angle,  $\Delta w_s$ , for two particles with differently sloped rotation curves. The  $\alpha = 1.5$  model has a rising rotation curve with a positive Lynden-Bell criterion value  $\mathcal{L}$  and  $\alpha = 3.0$  has a falling rotation curve with a negative  $\mathcal{L}$ . The  $\alpha = 1.5$  curve is multiplied by factor of 20 to show the oscillations which would be too small to see otherwise.

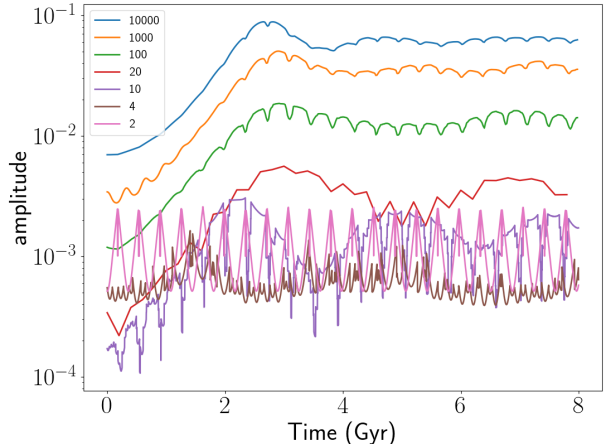


FIG. 14.— Bar amplitude as a function of particle number  $N$  for the NFW-like background model with  $\rho \propto r^{-1}$  in the vicinity of the particles. The amplitude is computed from a kernel density estimate of the distribution of  $w_s$  for the  $N$  particles.

system can be solved explicitly, using the well-known leapfrog algorithm or higher-order generalizations (Yoshida 1990). This approach works because the Hamiltonian can be separated or *split* into two pieces that depend only on  $\mathbf{q}$  or  $\mathbf{p}$ . For example, flows with  $H(\mathbf{q}, \mathbf{p}) = K(\mathbf{p})$  and  $H(\mathbf{q}, \mathbf{p}) = V(\mathbf{q})$  are both exactly solvable (see Sanz-Serna and Calvo 2018 for examples). To avoid an implicit method for the non-separable equations (B12)–(B13), we adopt the clever solution proposed by Tao (2016). Tao introduces an extended phase space with an *extra* copy of phase space  $(\mathbf{x}, \mathbf{y})$  that coincides with  $(\mathbf{q}, \mathbf{p})$  initially. The Hamiltonian of the extended system is the sum of three Hamiltonians:

$$\bar{H}(\mathbf{q}, \mathbf{p}, \mathbf{x}, \mathbf{y}) = H(\mathbf{q}, \mathbf{y}) + H(\mathbf{x}, \mathbf{p}) + \frac{\omega}{2} [(\mathbf{q} - \mathbf{x})^2 + (\mathbf{p} - \mathbf{y})^2]. \quad (\text{B15})$$

The first two terms are the original Hamiltonian function and the third term is a non-physical linear force that drives the two copies towards each other. One can solve each of the three Hamiltonians with an explicit method. Recall that an explicit symplectic ODE solver is a Hamiltonian map. The combined mapping for the three separable Hamiltonians in equation (B15) is the composition of three maps. The coupling parameter  $\omega$  needs to be chosen large enough to keep the two phase-space copies,  $(\mathbf{q}, \mathbf{p})$  and  $(\mathbf{x}, \mathbf{y})$ , close to each other but the solution is not sensitive to  $\omega$  once so tuned. Tao estimates that the error for a solution of length  $T$  is  $\mathcal{O}(Th^l\omega)$  for a duration  $\mathcal{O}(\min[h^{-l}\omega^{-1}, \omega^{1/2}])$  where  $l$  is the order using Yoshida (1990). Tao (2016) gives a detailed discussion of convergence and consistency. In practice, the Tao method produces high-accuracy solutions with little energy drift for the conservative time-independent system. However, unstable critical systems require large values of  $\omega$  and some tuning effort especially for  $N \lesssim 400$ . We compared our implementation of Tao’s algorithm to fourth-order Runge Kutta for verification. In practice, this method requires a much smaller time step than a traditional N-body code. The fourth-order ( $l = 4$ ) Tao method requires a comparable or larger number of function evaluations with similar long-term energy drift as fourth-order Runge Kutta at the same step size.

#### B.4. Test results

The simplest possible test of the new simulation method is the two-body quadrupole problem: two averaged particles that feel each other’s mutual potential along with the fixed monopole of the background system. This system is coupled pendulum and admits irregular motion. In the regular domain, the relative motion of the two interacting particles is oscillatory. Our first test solves equations (B12) and (B13) for  $N = 2$  and plots the the difference in  $w_s$ . The two particles have identical actions corresponding to a particles with  $J/J_{max}(E) = 0.8$  with guiding center radius of  $r_c = 3$  kpc; this corresponds to approximately one Milky-Way exponential scale length. The pericenter and apocenter of the unaveraged orbit is 0.006 and 0.012, respectively (1.8 and 3.6 kpc in Milky Way units, respectively). The initial position angles are displaced by 0.1 radians. The total mass of the two-particle system is  $2 \times 10^{-3}$  of the total background mass,  $M = 2 \times 10^9 M_\odot$ . These values are chosen to represent a typical ensemble of disk orbits in the vicinity of the disk scale length. None of these results depend qualitatively on this choice.

We consider two different background models (eq. 2): one with  $\alpha = 1.5, \beta = 0$  and one  $\alpha = 3.0, \beta = 0$  with the default values of  $r_t = 1.5, r_w = 0.2$  as described in Section 2.1.1. The Lynden-Bell criterion from equation (12) predicts that the first should bar *promoting* while the second should be bar *avoiding*. That is, the orbits will attract in the first case or *librate* and repel in the second case or *rotate*. Figure 13 presents the solutions of equations (B12) and (B13) and plots the the difference in  $w_s$ . This demonstrates the predicted behavior: the two particles librate for the  $\alpha = 1.5$  case which has  $\mathcal{L} > 0$  and rotate for the  $\alpha = 3.0$  case which has  $\mathcal{L} < 0$ .

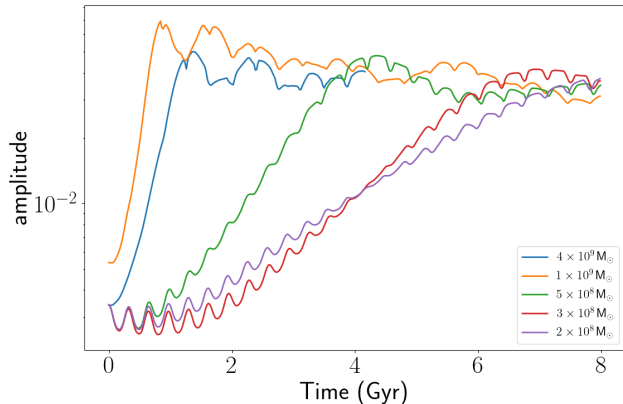


FIG. 15.— Bar amplitude variation as a function of disk mass, showing that the initial exponential growth is proportional to bar-particle mass. The model is the same as the one shown in Figure 14 and the total particle mass is shown in the legend.

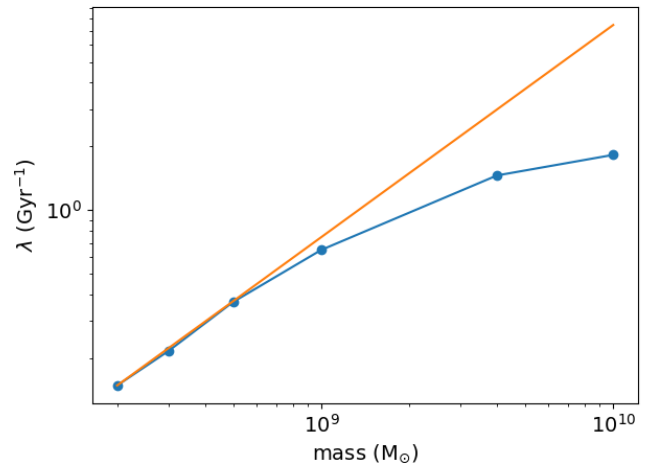


FIG. 16.— Exponential growth rate for the amplitude as a function of mass (blue) estimated from the curves in Fig. 15. The expected linear relation extrapolated from small mass is shown for comparison (orange). The expected linear scaling is only valid for small disk mass.

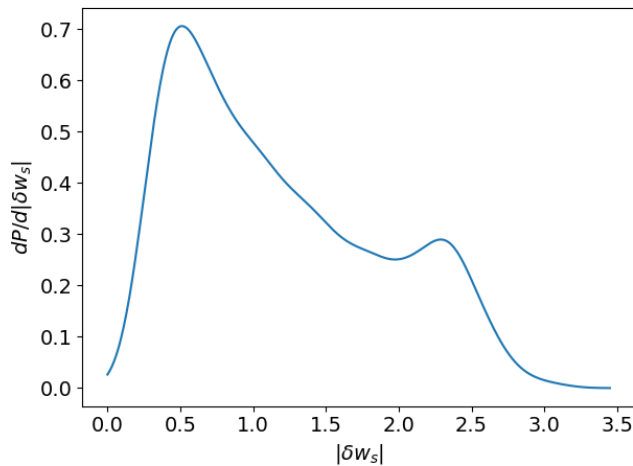


FIG. 17.— The distribution of the excursion angle,  $|\delta w_s|$ , in radians for the 9377 librating trajectories for the BarHMF run with  $N = 10000$  shown in Fig. 14. The excursion in apocentric position is  $|\delta w_s|/2$ . The apocentric distribution is approximately flat between  $10^\circ$  and  $70^\circ$  with a peak at  $20^\circ$ .

For  $N \gg 1$ , the particles can exchange slow action  $I_s$  with the mean field and thereby with each other. We use the extremum excursion of the probability distribution for the  $N$  values of  $w_s$  in the interval  $[0, 2\pi)$  to estimate the *amplitude* of the resulting bar. The distribution is constructed using a kernel density estimator with the optimal Gaussian kernel width expression from Silverman (1986). To explore the change in bar amplitude with time for simulations of various  $N$ , we choose an the NFW-like background model (eq. 2 with  $\alpha = 1, \beta = 2$ ). The model has  $\rho \propto r^{-1}$  in the vicinity of the BarHMF particles and is explicitly bar promoting according to  $\mathcal{L}$ . The particle parameters are the same as the two-particle model with the same total particle mass,  $M_b$ : particles have identical actions corresponding to a particles with  $J/J_{max}(E) = 0.8$  and a single guiding center radius of  $r_c = 0.01$ .

Figure 14 compares the bar amplitude from BarHMF runs with increasing values of  $N$ . The behavior for  $N = 2$  is sinusoidal libration as in Figure 13. For  $N \gtrsim 10$ , we begin to see a clear period of exponential growth followed by oscillation. As  $N$  increases, the amplitude increases with otherwise similar behavior: the classic bar-like exponential growth phase followed by a steady state. The short-period modulation of  $\approx 0.18$  is the one-particle libration time. This is corresponds to  $\sim 300$  Myr in Milky Way units. These modulations become weaker with increasing  $N$  as expected. This figure also shows a longer period modulation in the steady-state phase that decreases in amplitude and possibly increases in period with increasing  $N$ . We speculate that this is the ongoing phase mixing of transient from the initial formation but have not yet investigated this in detail.

The exponential growth rate seen in Figure 14 is nearly the same for all  $N \gtrsim 100$ . Indeed, we expect the growth

rate to depend on and increase linearly with total particle mass,  $M_b$ . Figure 15 demonstrates this with a sequence of simulations with  $N = 1000$  and varying mass with  $M_b$  between  $10^8 M_\odot$  and  $10^{10} M_\odot$ . The growth rate is estimated as the slope of the rise in the log-linear plot, shown in Figure 16. This slope is linearly proportional  $M_b$  until  $M_b \approx 10^9 M_\odot$ . For larger values, the slope increases more weakly with mass. For  $M_b \gtrsim 4 \times 10^9 M_\odot$  the increase in slope is weakly than linear, suggesting that bar is no longer following the linear predictions. Rather, it is growing as fast as it can limited by the intrinsic characteristic time of BarHMF model. The regime is typical of bar growth in unstable high-mass disks typical of N-body simulations of isolated galaxies.

For a final demonstration of the correspondence between the BarHMF and the full N-body simulations, we compare the fraction of trapped, librating orbits after bar formation is complete with the untrapped, rotating fraction. We do this by computing the difference between the position angle of each particle and the mean position angle of the entire ensemble as a function of time. The variation of the distribution around the ring is very close to sinusoidal. We use the same the probability distribution estimate of  $w_s$  used to infer the amplitude to find the position angle of the peak,  $\theta_{PA}$ . This yields a time series of excursions for the angle of each quadrupole particle relative to the bar position angle:  $\delta w_s(t) = w_s(t) - \theta_{PA}(t)$ . Then, we estimate the width of  $\delta w_s$  for each trajectory by computing the distance between the extremal values for all  $t$ , denoted as  $|\delta w_s|$ . A librating (rotating) trajectory has  $|\delta w_s|$  smaller (larger) than  $\pi$ . Using this to classify BarHMF trajectories, we find that 94% of the distribution is in libration by the end of the simulation at  $T = 4$  Gyr. Figure 17 shows the distribution of widths  $|\delta w_s|$  for the ensemble of librating trajectories. This distributions peaks at 0.7 rad (or  $40^\circ$ ) with a long heavy tail to large libration angle. This implies an excursion about the bar position at apocenter of  $|\delta w_s|/2$  or 0.35 rad (or  $20^\circ$ ). Petersen *et al.* (2021) find a similarly large trapped fraction of  $x_1$  orbits of approximately 80% in the bar vicinity. Moreover, the trapped BarHMF shows a broad tail of libration amplitudes which is also similar to the distributions seen in N-body simulations. A precise correspondence to the N-body simulations from Section 3 should not be expected for two reasons: (1) we have not included the background potential of the disk itself; and (2) we have not fully distributed the BarHMF particles according to the disk phase-space distribution function. Such simulations are possible but would require an intensive computational campaign that is beyond the scope of this preliminary study. Nonetheless, the good correspondence between the major features of bar growth and saturation suggest that the simple perturbation theory captures much of the bar instability mechanism and supplies a good model for further applications (Sec. B.5).

### B.5. Topics for future work

This paper focuses on the *classic*  $m = 2, l_1 = -1, l_2 = 2$  bar instability. Only one term in equations (B1) and (B2) is required. However, the BarHMF simulation can be trivially generalized to include multiple resonances ( $m, l_1, l_2$ ). The extended model can be used, for example, to explore non-linear resonance coupling in barred system in the non-linear regime. Technically, this requires adding multiple commensurabilities of the form in equation (B2) and eliminating averaging in favor of the full equations of motion for  $(\mathbf{w}, \mathbf{I})$ . For example, consider adding the classic 4:1 bar resonance (Contopoulos 1988). The pattern speed is the same for each harmonic:  $\Omega_p \equiv \Omega_{p2} = \Omega_{p4}$ . The commensurability is  $\Omega_r = 4(\Omega_\phi - \Omega_p)$  and gives a new term with  $m = 4, l_1 = -1, l_2 = 4$ . Each BarHMF particle now interacts with two shapes depending on its action values  $(I_r, I_\phi)$ : a dumbbell shaped quadrupole density and a 4-lobed octopole density (e.g. two pyramids joined at their bases or two orthogonally-oriented dumbbells). Each additional resonant term adds a new degree of freedom corresponding to the slow angle action from equation (B7). In addition, combinations with multiple  $m$  orders will have separate sets of coefficients for each order from equation (B14).

With one term, the BarHMF simulation is an ensemble of interacting pendula. This system is intrinsically irregular. Indeed some of the simulations described in Appendix B.4 show evidence of chaotic behavior. As we add more terms, we introduce the possibility additional chaotic channels such as resonance overlap (Chirikov 1979) and weak chaotic transport (Manos and Athanassoula 2011). The BarHMF model is ideal model for investigating the details of multiple resonance phenomena in barred systems. This ability to study the interactions of specific resonances is ideal for isolating and determining their relevance to barred systems in traditional simulations and Nature. With only several specific resonant terms, the computational effort will remain modest.

The examples in Appendix B.4 assume a spherical background potential for expediency and the same two-dimensional basis described in Appendix A and used for the simulations Section 3. We may couple the in-plane dynamics of the BarHMF model to other galactic components using the potential theory described in Appendix A. For example, we can study the evolution of the bar in the presence of dynamical friction and investigate the dependence on the dark-matter halo properties. The BarHMF model presents a new opportunity to understand the changes and redistribution of the bar orbits under torque, a subject which remains poorly understood dynamically. This exploration might be especially productive with BarHMF which provides the opportunity to explicitly identify interactions between multiple resonances.

This paper was built using the Open Journal of Astrophysics L<sup>A</sup>T<sub>E</sub>X template. The OJA is a journal which provides fast and easy peer review for new papers in the `astro-ph` section of the arXiv, making the reviewing process simpler for authors and referees alike. Learn more at <http://astro.theoj.org>.